

MOLECULAR GAS AND NUCLEAR ACTIVITY IN RADIO GALAXIES DETECTED BY *IRAS*

A. S. EVANS^{1,2}, J. M. MAZZARELLA³, J. A. SURACE⁴, D. T. FRAYER⁴, K. IWASAWA⁵, & D. B. SANDERS^{6,7}

Draft version October 29, 2018

ABSTRACT

This paper reports the latest results from a millimeter-wave (CO) spectroscopic survey of IRAS-detected radio galaxies with $L_{1.4\text{GHz}} \sim 10^{23-28}$ W Hz⁻¹ in the redshift range $z \sim 0.02 - 0.15$. The IRAS flux-limited sample contains 33 radio galaxies with different radio morphologies and a broad range of infrared luminosities ($L_{\text{IR}} = 10^{9-12} L_{\odot}$), allowing for an investigation of (a) whether low- z radio-selected AGN reside in molecular gas-rich host galaxies, and (b) whether the CO properties are correlated with the properties of the host galaxy or the AGN. All of the radio galaxies in Mazzarella et al. (1993) and Mirabel et al. (1989) have been reobserved. Three new CO detections have been made, raising the total number of CO detections to nine and setting the survey detection rate at $\sim 25\%$. Many of the CO lines have double-peaked profiles, and the CO line widths are broad (average $\Delta v_{\text{FWHM}} \sim 500 \pm 130$ km s⁻¹), exceeding the average CO widths of both ultraluminous infrared galaxies (300 ± 90 km s⁻¹) and Palomar-Green QSOs (260 ± 160 km s⁻¹), and thus being indicative of massive host galaxies. The CO luminosities translate into molecular gas masses of $\sim 0.4 - 7 \times 10^9 M_{\odot}$, however, the 3σ CO upper limits for nondetections do not rule out a molecular gas mass as high as that of the Milky Way ($\sim 3 \times 10^9 M_{\odot}$). Optical images of eight out of nine molecular gas-rich radio galaxies show evidence of close companions and/or tidal features. Finally, there is no obvious correlation between radio power and molecular gas mass. However, it is notable that only one F-R II galaxy out of 12 is detected in this CO survey; the remaining detections are of galaxies hosting F-R I and compact radio jets.

Subject headings: galaxies: active — galaxies: interacting — galaxies: ISM — ISM: molecules — infrared: galaxies —

1. INTRODUCTION

A connection between galaxy-galaxy mergers and the onset of nuclear activity in classical optical and radio-selected Active Galactic Nuclei (AGN) has been inferred over the last 20 years. Many classical radio galaxies and QSOs have been observed at optical and near-infrared wave-

lengths to have double-nuclei, tidal bridges/tails, and close companions consistent with them being the mergers of disk galaxies (e.g. Stockton & MacKenty 1983; Heckman et al. 1986; Smith & Heckman 1990a,b; McLeod & Rieke 1994; Surace, Sanders & Evans 2001). Further evidence of the AGN-merger connection has resulted from multi-

¹Department of Physics & Astronomy, Stony Brook University, Stony Brook, NY, 11794-3800: aevans@mail.astro.sunysb.edu

²Visiting Astronomer at the Infrared Processing & Analysis Center, California Institute of Technology, MS 100-22, Pasadena, CA 91125

³Infrared Processing & Analysis Center, California Institute of Technology, MS 100-22, Pasadena, CA 91125: mazz@ipac.caltech.edu

⁴SIRTF Science Center, California Institute of Technology, Pasadena, CA 91125: jason@ipac.caltech.edu

⁵Institute of Astronomy, Madingley Road, Cambridge CB3 0HA

⁶Institute for Astronomy, 2680 Woodlawn Dr., Honolulu, HI 96822: sanders.ifa.hawaii.edu

⁷Max-Plank Institut fur Extraterrestrische Physik, D-85740, Garching, Germany

wavelength surveys of luminous infrared-selected galaxies, which have shown these galaxies to be merging/interacting disk galaxies and have shown an increasing fraction of infrared galaxies with optical, near-infrared, and X-ray signatures of imbedded AGN as a function of increasing luminosity (e.g., Sanders et al. 1988a,b; Veilleux, Sanders, & Kim 1997, 1999; Veilleux et al 1999; Vignati et al. 1999).

Star formation appears to be a component of the activity occurring in the host galaxies of AGN – a growing number of radio galaxies and QSOs have detectable amounts of molecular gas and young UV-luminous knots indicative of recent star formation (Philips et al. 1987; Sanders, Scoville, & Soifer 1988c; Lazareff et al. 1989; Mirabel, Sanders, & Kazès 1989; Mazzarella et al. 1993 – hereafter, Paper 1; Reuter et al. 1993; Evans et al. 2001; Allen et al. 2002; Scoville et al. 2003). In addition, the fraction of classical AGN with dust in their host galaxies is substantial (e.g., Golombek et al. 1988; Sanders et al 1989), with $\sim 50\%$ of 3C radio galaxies and $\sim 70\%$ of Palomar-Green (PG: Schmidt & Green 1983) QSOs at $z \lesssim 0.12$ having IRAS⁸ detections at $60\mu\text{m}$. The Infrared Space Observatory (ISO) detected thermal dust emission in a larger fraction of radio galaxies and QSOs (Meisenheimer et al. 2001; Haas et al. 2003, 2004), providing further proof of rich ISMs in the host galaxies of radio galaxies and QSOs. This dust is most likely a combination of dust intrinsic to the progenitor galaxies, as well as dust produced through stellar mass loss from a recent/ongoing starburst.

The importance of star formation in AGN host galaxies is also inferred via recent black hole surveys in nearby galaxies. These observations have shown that the massive spheroidal component of many nearby normal galaxies contain quiescent supermassive nuclear black holes ($M_\bullet = 10^{6-9} M_\odot$: e.g. Magorrian et al. 1998). A key result that has come from these surveys is the scaling of black hole mass with stellar bulge mass (e.g., Magorrian et al. 1998). Such a correlation may indicate that the formation of stars in the bulge component of galaxies is intimately associated with the building of supermassive black holes.

While the molecular gas properties of infrared-selected galaxies have been studied in detail, CO

observations of large samples of radio galaxies and QSOs have lagged behind. Thus, conclusions about the CO properties of classical AGN and their host galaxies is often based on small number statistics or incomplete data sets. The present study focusses on the global molecular gas properties of a sample of low-redshift radio galaxies, and it serves as an extension of the survey presented in Paper 1. The primary issues to be addressed with this survey are (a) whether low- z radio-selected AGN reside in molecular gas-rich host galaxies and (b) whether the CO properties are correlated with the properties of the host galaxy or the AGN. To address the latter issue, the millimeter data are complemented by infrared, radio, and X-ray data to allow a comparison between the available amount of fuel for star formation (and perhaps AGN activity) and the energy emitted from the AGN and/or host galaxy at these wavelengths. The analysis presented here builds primarily upon similar analysis done of low-redshift, infrared-selected galaxies over the last twenty years (e.g., Sanders & Mirabel 1996 and references therein; Franceschini et al. 2003; Trentham et al. 2005) and recent analysis of a sample of CO-detected PG QSO host galaxies (Evans et al. 2001). These galaxies, which may emanate from the same parent population as the radio galaxies or be linked via evolution, will serve as the primary comparison samples. In addition, optical imaging of a radio galaxy sub-sample will be briefly discussed. Parts of this extended millimeter survey have been presented elsewhere (Evans 1996; Sanders & Mirabel 1996; Evans 1998; Evans et al. 1999a,b).

This paper is divided into six sections. The selection criteria of the radio galaxy sample is discussed in §2. Section 3 is a summary of the observations and data reduction. In §4, the CO($1 \rightarrow 0$) emission-line properties are presented, along with the method of calculating the molecular gas mass. Section 5 contains a brief summary of the optical imaging data and an extended discussion of the infrared, radio, CO, and X-ray properties of the radio galaxies relative to those of infrared-selected galaxies, PG QSOs, and elliptical galaxies. Section 6 is a summary. Throughout the paper, $H_0 = 75 \text{ km s}^{-1} \text{ Mpc}^{-1}$, $q_0 = 0.5$, and $\Lambda = 0.0$ are assumed.

2. SAMPLE

⁸I.e., the Infrared Astronomical Satellite.

The radio galaxy sample was selected primarily from a list of radio galaxies correlated with the IRAS archive by Golombek, Miley & Neugebauer (1988). The radio galaxies were selected for CO observations based on the following criteria: (i) a declination, $\delta > -20^\circ$, to allow observations from both the Kitt Peak 12m Telescope and the James Clerk Maxwell Telescope (JCMT), (ii) *IRAS* flux densities at $60\mu\text{m}$, $f_{60\mu\text{m}}$, or $100\mu\text{m}$, $f_{100\mu\text{m}}$, greater than 0.3 Jy, with the assumption that an *IRAS* detection at this level is a good indicator of a dusty, gas-rich interstellar medium, and (iii) a redshift in the range $0.02 \lesssim z \lesssim 0.15$, to ensure detectability of the molecular gas mass of the Milky Way ($\sim 3 \times 10^9 M_\odot$), if present, with single-dish millimeter telescopes used for the survey (for the sensitivity calculation, the assumption is made that the CO lines have a full width at half the maximum intensity width of $\Delta v_{\text{FWHM}} \sim 250 \text{ km s}^{-1}$, which is the average value for a sample of *IRAS* galaxies observed by Sanders, Scoville, & Soifer 1991). Such criteria yield 31 radio galaxies. Two additional radio galaxies, PKS 0624-20 and 3C 285, were identified via a search of the NASA Extragalactic Database (NED) to have properties consistent with the selection criteria; their addition to the sample raises the total number of galaxies to 33. Note that two of the 33 galaxies, the relatively nearby galaxies NGC 6251 and 3C 272.1, have CO non-detections in published surveys by Elfhag et al. (1996) and Knapp & Rupen (1996), and thus were not reobserved as part of this survey. General properties of the sample of 33 radio galaxies are provided in Table 1.

3. OBSERVATIONS AND DATA REDUCTION

3.1. CO Spectroscopy

Millimeter observations of the redshifted CO($1 \rightarrow 0$) emission in 31 of the 33 radio galaxies were made with the NRAO⁹ 12m Telescope during six observing periods between 1992 December and 2000 June. The telescope was configured with two 256×2 MHz channel filterbanks and dual polarization SIS spectral-line receivers tuned to the frequency corresponding to the redshifted CO($1 \rightarrow 0$) emission line. (Optical emission line redshifts were adopted.) Observations were obtained using a nutating subreflector with a chop rate of ~ 1.25 Hz. Six minute scans were taken, and a calibration was done every other scan. Dur-

ing the course of each observation, data were also taken with the bandpass centered at velocity offsets of ± 20 or 50 km s^{-1} of the velocity corresponding to the redshift of the optical emission lines. Shifting the velocities in such a manner minimizes any ripples inherent in the baseline. Pointing was checked every few hours by observing standard continuum sources and was generally determined to be accurate to within a few arcseconds.

Observations of the redshifted CO($1 \rightarrow 0$) emission in Cygnus A and PKS 1345+12 were done at the IRAM 30m telescope during 1995 December and 2003 December observing periods, respectively. The 3 and 1 millimeter receivers were used simultaneously in combination with the filterbanks and an autocorrelator to provide bandwidths of 512 and 600 MHz, respectively. During observations, the pointing was monitored by observing the planets and standard continuum sources.

Observations of the redshifted HCN($1 \rightarrow 0$) emission in PKS 0502-10 and B2 0722+30 were done at the IRAM 30m telescope during the 2003 December observing period. The setup was identical to the CO($1 \rightarrow 0$) observation of PKS 1345+12 obtained during the same period. HCN observations of the strong 3mm continuum galaxies 3C 84 and 3C 120 were also attempted, but have been left out of the present discussion due to the presence of large baseline ripples in the data.

Observations of the redshifted CO($2 \rightarrow 1$) emission in PKS 0502-10 and B2 0722+30 were done with the James Clerk Maxwell Telescope (JCMT) in 1995 September. The spectral line receiver (A2) were used together with the Digital Auto-correlation Spectrometer in wide-band mode (750 MHz bandwidth). Because of excess noise near the edge of the passband, the usable bandwidth was only ~ 700 MHz, which corresponds to a total velocity coverage of $\sim 900 \text{ km s}^{-1}$ at 230 GHz. All observations were obtained using a nutating subreflector with a chop rate of ~ 1.25 Hz. Data were stored as six-minute scans, and a chopped wheel calibration was performed after every other scan. Pointing was monitored every few hours, and velocity shifts of $\pm 20 \text{ km s}^{-1}$ were made to minimize baseline ripples. A journal of observations for all of the single-dish observations are provided

⁹The NRAO is a facility of the National Science Foundation operated under cooperative agreement by Associated Universities, Inc.

in Table 2.

The data reduction for all of the single-dish millimeter and submillimeter observations were reduced using the IRAM data reduction package CLASS. The individual scans were checked for baseline instabilities, then averaged together. A linear baseline was subtracted from each spectrum; the cases where emission lines were detected, the baseline subtraction was done at velocities outside of the range of the emission line. Each spectrum was smoothed to $\sim 20-50$ km s $^{-1}$. Finally, line fluxes were measured by numerically integrating over the channels in the line profile, and the line widths were measured as full width at 50% of the peak flux. The resultant spectra are plotted in Figures 1–3.

3.2. Optical Imaging

Ground-based imaging observations of 7 of the radio galaxies in the sample were made at the UH 2.2m Telescope. The U', B, and I-band images were obtained over the period 1998 March 25 to 2000 December 31 using the Orbit Semiconductor 2048 \times 2048 CCD camera. The original scale is 0.09''/pixels (Wainscoat 1996), but the CCD was read out with 2 \times 2 pixel binning. Three to four dithered exposures were taken, with integration times ranging from 360 to 720 seconds each for U', B, and I-band filters.

The U', B, and I-band data reduction was performed using IRAF. The data reduction consisted of flatfielding individual images, scaling each image to its median value to correct for offsets in individual images, then shifting and median combining the images. The final images, boxcar smoothed by 4 \times 4 pixels, are shown in Figure 4.

4. RESULTS

Table 3 is a summary of the CO emission-line properties of the 31 radio galaxies observed as part of this survey. All of the radio galaxies observed for Paper 1 were reobserved, as well as two additional radio galaxies previously detected in CO (3C 84: Lazareff et al. 1989; Mirabel et al. 1989; Reuter et al. 1993, PKS 1345+12: Mirabel et al. 1989). In one case (TXS 1506+345), the pointing was shifted by $\sim 30''$ from that used in Paper 1 in order to center the galaxy in the beam. Nine radio galaxies are detected in CO(1 \rightarrow 0),

including three new detections (3C 31, PKS 0502-10, 3C 293)¹⁰. However, the previously reported detection of CO emission in B2 0648+27 was not confirmed. The radio galaxy PKS 1345+12 was the weakest CO detection in the sample, thus independent CO observations of the galaxy were also obtained with the IRAM 30m Telescope to improve the determination of the CO flux and line shape (Figure 1b). The average full width at half the maximum intensity velocity, Δv_{FWHM} , of the detected galaxies is 500 km s $^{-1}$. Several of the galaxies have double-peaked profiles.

Table 3 lists the measured CO intensities and luminosities. The CO luminosities of 3C 120, B2 0722+30, B2 1318+34, and TXS 1506+345 agree with the values in Paper 1 to within $\sim 20\%$, and the values of Δv_{FWHM} for all except TXS 1506+345 are similar (TXS 1506+345 is reported as having a 2-component CO emission line profile in Paper 1). There is a major discrepancy between the new CO measurements of Perseus A and PKS 1345+12 and those in the literature. For Perseus, the line width of CO luminosity are in agreement with the measurements of Lazareff et al. 1989 and Reuter et al. (1993), but L'_{CO} is a factor of two higher than the value determined by Mirabel et al. (1989). The discrepancy with the Mirabel et al. (1989) measurements results from what appears to be extended emission in the wings of the line in Figure 1 – if this emission is ignored, then the CO luminosity is 6×10^8 K km s $^{-1}$ pc 2 , within 22% of the value reported by Mirabel et al. (1989). The PKS 1345+12 CO luminosity comparison is more difficult to rectify – the CO luminosity is a factor of two lower than measured by Mirabel et al. (1989). Note, however, that the errors associated with the Mirabel et al. (1989) data are not known. The present PKS 1345+12 CO measurements are correct to within the error of those reported in Evans et al. (1999) if a 20% calibrated error on the present observations is assumed.

Many of the observations resulted in non-detections. For each of these galaxies, upper limits to the CO intensity were calculated via,

$$T_{\text{mb}}\Delta v < \frac{3T_{\text{rms}}\Delta v_{\text{FWHM}}}{\sqrt{\Delta v_{\text{FWHM}}/\Delta v_{\text{res}}}} \quad [\text{K km s}^{-1}], \quad (1)$$

where T_{mb} is the main beam temperature,

¹⁰Note that a detection of 3C 31 has also been reported by Lim et al. (2000).

Δv_{FWHM} is the average FWHM velocity for the detected radio galaxies ($= 500 \text{ km s}^{-1}$), and T_{rms} is the root-mean-squared main beam temperature of the spectral data for a velocity resolution of Δv_{res} .

To calculate the CO luminosity, the luminosity distance for a source at a given redshift and a $\Lambda = 0$ Universe was first calculated using the equation

$$D_L = cH_0^{-1}q_0^{-2} \left\{ zq_0 + (q_0 - 1) \left(\sqrt{2q_0z + 1} - 1 \right) \right\} [\text{Mpc}]. \quad (2)$$

Given the measured CO flux, $S_{\text{CO}}\Delta v$ [Jy km s^{-1}], the CO luminosity of a source at redshift z is

$$L'_{\text{CO}} = \left(\frac{c^2}{2k\nu_{\text{obs}}^2} \right) S_{\text{CO}}\Delta v D_L^2 (1 + z)^{-3} [\text{K km s}^{-1} \text{ pc}^2], \quad (3)$$

(Solomon, Downes, & Radford 1992) where c [km s^{-1}] is the speed of light, k [J K^{-1}] is the Boltzmann constant, and ν_{obs} [Hz] is the observed frequency. In terms of useful units, $L'_{\text{CO}(1 \rightarrow 0)}$ can be written as

$$L'_{\text{CO}} = 2.4 \times 10^3 \left(\frac{S_{\text{CO}}\Delta v}{\text{Jy km s}^{-1}} \right) \left(\frac{D_L}{\text{Mpc}} \right)^2 (1 + z)^{-1} [\text{K km s}^{-1} \text{ pc}^2]. \quad (4)$$

To estimate the mass of molecular gas in these radio galaxies, the reasonable assumption that the CO emission is optically thick and thermalized, and that it originates in gravitationally bound molecular clouds, is made. Thus, the ratio of the H_2 mass and the CO luminosity is given by

$$\alpha = \frac{M(\text{H}_2)}{L'_{\text{CO}}} \propto \frac{\sqrt{n(\text{H}_2)}}{T_b} [\text{M}_\odot (\text{K km s}^{-1} \text{ pc}^2)^{-1}], \quad (5)$$

where $n(\text{H}_2)$ and T_b are the density of H_2 and brightness temperature for the $\text{CO}(1 \rightarrow 0)$ transition (Scoville & Sanders 1987; Solomon, Downes, & Radford 1992). Multitransition CO surveys of molecular clouds in the Milky Way (e.g. Sanders et al. 1993), and in nearby starburst galaxies

(e.g. Güsten et al. 1993) have shown that hotter clouds tend to be denser such that the density and temperature dependencies cancel each other. The variation in the value of α is approximately a factor of 2 for a wide range of kinetic temperatures, gas densities, and CO abundance (e.g. $\alpha = 2 - 5M_\odot$ [$\text{K km s}^{-1} \text{ pc}^2$] $^{-1}$: Radford, Solomon, & Downes 1991). Solomon et al. (1997) and Downes & Solomon (1998) have made use of dynamical mass estimates of a low-redshift infrared galaxy sample observed in CO with the Plateau de Bure Interferometer to argue that α may, in some cases, be as low as $1 M_\odot$ ($\text{K km s}^{-1} \text{ pc}^2$) $^{-1}$.

For the present sample of galaxies, an $\alpha = 1.5M_\odot$ ($\text{K km s}^{-1} \text{ pc}^2$) $^{-1}$ is adopted, which is the approximate value derived for luminous and ultraluminous infrared galaxies (Solomon et al. 1997; Downes & Solomon 1998; Evans et al. 2002). However, note that α for some, or all, of these galaxies may be a factor of 2 – 3 higher (i.e., the approximate value derived for bulk of the molecular gas in the disk of the Milky Way: Scoville & Sanders 1987; Strong et al. 1988). The derived molecular gas masses are listed in Table 3. Taking these masses and comparing them with the dust masses, M_{dust} , which are calculated via

$$M_{\text{dust}} \sim 4.78 \left(\frac{f_{100\mu\text{m}}}{\text{Jy}} \right) \left(\frac{D_L}{\text{Mpc}} \right)^2 \left(e^{143.88/T_{\text{dust}}} - 1 \right) [\text{M}_\odot] \quad (6)$$

(see Young et al. 1989) where the dust temperature, T_{dust} is calculated from the $60\mu\text{m}$ and $100\mu\text{m}$ flux densities via

$$T_{\text{dust}} = -(1 + z) \left[\frac{82}{\ln(0.3f_{60\mu\text{m}}/f_{100\mu\text{m}})} - 0.5 \right] [\text{K}], \quad (7)$$

yields an average molecular gas-to-dust mass ratio of 860 ± 460 (see Table 4). By comparison, the gas-to-dust ratio is ~ 600 ($\alpha = 4.8M_\odot$ [$\text{K km s}^{-1} \text{ pc}^2$] $^{-1}$) for IRAS-detected spiral and luminous infrared galaxies (Young & Scoville 1991 and references therein). Note that the estimated dust masses in Table 4 are likely lower limits; the bulk of the dust in these galaxies may be in a colder ($< 30\text{K}$) dust component (Young & Scoville 1991; Devereux & Young 1990).

Given the adopted value of α , it is worthwhile to make a conservative estimate of the dynamical mass in order to determine the percentage of the total mass in the form of molecular gas. The dynamical mass within the region of the galaxies containing molecular gas and dust can be calculated via

$$M_{\text{dyn}} \sim \frac{\Delta v_{\text{FWHM}}^2 R_{\text{CO}}}{G} = 226 \left(\frac{\Delta v_{\text{FWHM}}}{\text{km s}^{-1}} \right)^2 \left(\frac{R}{\text{pc}} \right) [\text{M}_{\odot}], \quad (8)$$

where Δv_{FWHM} is the full CO velocity width at half the maximum flux density (Table 3) and R_{CO} is the radius of the CO distribution. The quantity R_{CO} is estimated by assuming optically thick, thermalized gas with a unity filling factor and a blackbody temperature, T_{bb} , equal to that of the dust. Thus, the radius of the CO distribution is calculated via

$$R_{\text{CO}} = \sqrt{\frac{L'_{\text{CO}}}{\pi T_{\text{bb}} \Delta v_{\text{FWHM}}}} \text{ [pc]} \quad (9)$$

(see Table 4). The resultant size estimates yield $M_{\text{dyn}} \sim 0.22 - 2.5 \times 10^{10} \text{ M}_{\odot}$ and thus $M(\text{H}_2)/M_{\text{dyn}} = 0.10 - 0.94$ with a mean value of 0.45 ± 0.29 .

Note that the values of R_{CO} are likely to be underestimated, and thus the derived values of $M(\text{H}_2)/M_{\text{dyn}}$ are lower limits. For example, the column densities derived from R_{CO} and $M(\text{H}_2)$ are in the range $1 - 4 \times 10^{24} \text{ cm}^{-2}$. In contrast, the X-ray column densities estimated from X-ray observations of 3C 120 and PKS 1345+12 are in the range of $0.2 - 4 \times 10^{22} \text{ cm}^{-2}$ (Sambruna et al. 1999; O'dea et al. 2000). Further, the CO disks in 3C 293 (Evans et al. 1999a) and 3C 31 (Okuda et al. 2005) are extended ~ 6 kpc and 1 kpc, respectively, which are 6–12 times the sizes of the respective CO distributions listed in Table 4. This issue will be addressed further in a follow-up paper containing CO interferometric maps of the sample (Evans et al. 2005a).

5. DISCUSSION

The present CO survey has increased the number of radio galaxies observed in Paper 1 by a factor of four. Three new CO detections have been made, yielding a 25% detection efficiency for the sample with the 12m telescope. The CO

detections translate into molecular gas masses of $0.4 - 7 \times 10^9 \text{ M}_{\odot}$, with 3σ upper limits for non-detections in the range of $< 4 \times 10^8 \text{ M}_{\odot}$ for a $z \sim 0.02$ galaxy to $< 3.3 \times 10^9 \text{ M}_{\odot}$ for a $z \sim 0.1$ galaxy. Thus, while only a quarter of the sample was detected, the upper limits of the more distant members of the sample do not rule out molecular gas mass as high as that of the Milky Way ($\sim 3 \times 10^9 \text{ M}_{\odot}$).

There are two notable features in the CO spectra shown in Figure 1. The first is the broad linewidth – the average Δv_{FWHM} of the present sample of radio galaxies is $\sim 500 \pm 130 \text{ km s}^{-1}$, which exceeds the average value for both PG QSOs ($260 \pm 160 \text{ km s}^{-1}$: Evans et al. 2005b) and ultraluminous infrared galaxies ($300 \pm 90 \text{ km s}^{-1}$: Solomon et al. 1997) detected in CO to date. This result likely indicates that the host galaxies of molecular gas-rich radio galaxies are extremely massive. The second notable feature is the double-peaked CO emission line profiles in many of the spectra. Interferometric CO observations of two of these galaxies are in the literature and show this feature to be present for (at least) two different reasons. In the case of 3C 293, the “double-peak” appearance is caused by a CO absorption feature at the systemic velocity of the galaxy (Evans et al. 1999a). In the case of 3C 31, the molecular gas is distributed in a ring (Okuda et al. 2005).

Figure 4 shows optical images of 7 of the nine radio galaxies detected in CO; two of the nine radio galaxies (B2 1318+34 and PKS 1345+12) are well-studied systems that have been imaged by several groups (e.g. Sanders et al. 1988b; Bushouse & Stanford 1992; Surace et al. 1998; Evans et al. 1999b; Scoville et al. 2000; Kim, Veilleux, & Sanders 2003), and thus have not been reobserved by us. Most of these molecular gas-rich galaxies have nearby companions (3C 31; PKS 1345+12) and/or show clear evidence of being involved in a recent merger (3C 84; 3C 120; PKS 0502-10; 3C 293; PKS 1345+12; B2 1318+34). The one exception is B2 0722+30, an edge-on spiral galaxy. While the images in Figure 4 support the possibility that interaction and merger events may be a primary trigger for radio-loud AGN activity, it is notable that many low-redshift radio galaxies are elliptical galaxies (e.g., Sandage 1966; Martel et al. 1999). Thus, unless the elliptical galaxies are advanced mergers, other mechanisms must play an important role in ignit-

ing the AGN activity observed in these galaxies.

Given the results of the present survey and recent CO surveys of low-redshift PG QSOs (Evans et al. 2001; Scoville 2003), there is sufficient data to begin a comparison of the molecular gas properties and the global energy output (measured at infrared, radio, and X-ray wavelengths) of classical UV and radio-selected AGN with infrared-selected galaxies and elliptical galaxies. Before exploring such comparisons, it is worth first considering two issues which have direct relevance to the interpretation of the data. The first issue is the infrared bias in the sample. While the sample was selected based on the $60\mu\text{m}$ and $100\mu\text{m}$ flux densities, it is important to realize that (a) the flux density limits are extremely low, and thus the infrared luminosity range of the sample spans several decades (i.e., $L_{\text{IR}} \sim 10^{9-12} L_{\odot}$), and that (b) 55%, 33%, and 24% of $z \lesssim 0.1$ 3C, B2 and PKS galaxies, respectively, were detected at $60\mu\text{m}$ by IRAS. The fraction for PG QSOs is even higher, with 69% of PG QSOs out to $z \sim 0.17$ (the redshift limit of the QSO CO survey) having $60\mu\text{m}$ detections. Thus, infrared excesses in AGN host galaxies from radio-selected (and UV-selected) surveys are quite common.

The second issue of relevance to the interpretation of the data is the nature of the radio emission from the galaxies in the sample; i.e., whether the radio emission from all of the galaxies in the sample is due to AGN jet emission, or whether some of the galaxies are actually nearby starburst galaxies luminous enough in the radio to have been detected by the 3C, B2 or PKS surveys. To address this issue, IRAS and 1.4 GHz data have been compiled for the radio galaxies, along with complementary data sets for infrared galaxies with both warm and cool 25-to- $60\mu\text{m}$ colors (note that classical AGN typically have warm colors, $f_{25\mu\text{m}}/f_{60\mu\text{m}} > 0.2$), PG QSOs, and elliptical galaxies. Figure 5 shows the result of the compilation; plotted is the 1.4 GHz-to-infrared luminosity ratio, $L_{1.4\text{GHz}}$, versus the infrared luminosity, L_{IR} . The “radio-infrared” correlation (see Condon 1992) is clearly visible in this Figure; the radio-to-infrared ratio for infrared-selected galaxies is relatively constant with increasing infrared luminosity. This has led to speculation that the same population of massive stars responsible for heating the dust is also responsible for the radio emission (through, for example, the production of supernovae). Lonsdale, Smith,

& Lonsdale (1995) showed that QSOs follow the same bolometric luminosity–radio correlation as infrared galaxies. Similarly, the QSOs follow the infrared–radio correlation in Figure 5, indicating, perhaps, that a significant fraction of their radio and infrared emission is associated with massive stars, or that AGN-related processes in radio-quiet sources yield the proper $L_{1.4\text{GHz}}/L_{\text{IR}}$ ratio to place QSOs on the relation. In contrast, the data points for all but one of the radio galaxies are above this correlation; their excess radio emission is associated with AGN jets. Only the galaxy B2 1318+34 (aka IC 883), which is classified optically as a LINER galaxy, has a $L_{1.4\text{GHz}}/L_{\text{IR}}$ ratio consistent with the infrared–radio correlation. The LINER classification is commonly an indication of ionization of an AGN with a shallow power law, however, the spatial coincidence between the radio (Condon et al. 1991) and CO (Downes & Solomon 1998) emission in the disk of IC 883 is evidence in favor of the radio emission being associated with a starburst population. Given this, B2 1318+34 will be denoted by a symbol different from the other radio galaxies in Figures 6 and 8.

5.1. Global CO-Infrared Properties

Figure 6 shows two common plots of infrared and CO luminosity for extragalactic sources. The first plot is the CO luminosity versus the infrared luminosity of the radio galaxies and PG QSOs, plotted with infrared galaxies and elliptical galaxies with CO detections. In addition, arrows have been plotted to represent $3\sigma L'_{\text{CO}}$ upper limits for the radio galaxies with CO nondetections in the present survey. There are two noteworthy features in Figure 6a. First, the PG QSO population appear to have low CO luminosities for their infrared luminosity relative to infrared galaxies (see also Evans et al. 2001). Second, by contrast, the radio galaxies are well distributed throughout the area of the plot occupied by infrared and elliptical galaxies, with the three newly detected radio galaxies (3C 31, PKS 0502-10, and 3C 293) having high CO luminosities for their infrared luminosity. These features are better represented in Figure 6b, which is a plot of the $L_{\text{IR}}/L'_{\text{CO}}$ versus the infrared luminosity. The ratio $L_{\text{IR}}/L'_{\text{CO}}$ is commonly referred to as the star formation efficiency, i.e., it is the measure of energy from massive stars heating the dust normalized by the amount of molecular gas available to form new stars. Thus, for highly efficient starbursts (i.e.,

high $L_{\text{IR}}/L'_{\text{CO}}$), a large number of massive stars are produced from the available gas. The QSOs have high $L_{\text{IR}}/L'_{\text{CO}}$, indicating that either they are producing massive stars with extremely high efficiency, or that there is significant heating of the dust by the AGN (Evans et al. 2001). Most of the radio galaxies have $L_{\text{IR}}/L'_{\text{CO}}$ similar to those of giant molecular clouds (GMCs: Sanders & Mirabel 1996) in the Galaxy. Exceptions to this include PKS 1345+12, which has a $L_{\text{IR}}/L'_{\text{CO}}$ similar to the PG QSOs, and the three newly detected radio galaxies, which have $L_{\text{IR}}/L'_{\text{CO}}(< 30)$ similar to the global value for local spiral galaxies (see also Evans et al. 1999a).

It thus appears that while some radio galaxies have significant amounts of molecular gas, the rate of massive star formation is extremely low. Indeed, if the assumption is made that the infrared luminosity in 3C 31, PKS 0502-10, and 3C 293 is due entirely to star formation, then the star formation rates are roughly a few solar masses per year. Note also that the dust temperatures of 3C 31, PKS 0502-10, and 3C 293 are lower (30–45 K) than that of the previously detected radio galaxies (55–90 K), also consistent with the idea that current massive star formation rates in these three radio galaxies is low.

5.2. Global X-ray Properties

Given the amount of molecular gas in the radio galaxies detected in CO to date, and the diversity in the apparent levels of active star formation (as traced by L_{IR} and $L_{\text{IR}}/L'_{\text{CO}}$), it is worth examining their hard (2–10 keV) X-ray properties to determine (a) whether these radio galaxies have X-ray emission indicative of AGN, and (b) whether any of the radio galaxies have sufficient column densities of molecular gas to be significantly X-ray absorbed. The L_{X} -to- L_{FIR} ratio provides a straight-forward way of addressing these issues – the ratio is constant in starburst galaxies, indicating that the starburst responsible for heating the dust in HII region galaxies produces a constant fraction of massive X-ray binary pairs (Grimm et al. 2003; Ranalli et al. 2003). ‘Excesses’ in $L_{\text{X}}/L_{\text{FIR}}$ arise from the contribution of AGN to the X-ray emission, making the ratio a powerful AGN vs. starburst diagnostic. However, in objects that contain large columns of gas and dust, the X-ray emission can be suppressed, lowering the observed $L_{\text{X}}/L_{\text{FIR}}$.

For the purposes of the present discussion, the

available radio galaxy data of our sample have been compiled from the literature and added to the L_{X} vs. L_{FIR} plot of Trentham et al. (2005), which is a compilation of data of local LINERs, Seyferts, HII-region galaxies, infrared galaxies, and PG QSOs. The result is plotted in Figure 7; Figure 7a shows the data plotted in the manner typically done by other authors, i.e., L_{X} vs. L_{FIR} , and Figure 7b shows the data plotted in terms of the $L_{\text{X}}/L_{\text{FIR}}$ versus L_{FIR} . A least-squares fit has been applied to the HII region galaxy data. Several of the infrared galaxies, which are rich in molecular gas, are below the fit and thus Compton thick. In terms of the radio galaxies data, the Figures show that, (a) the AGN dominates the X-ray emission from the radio galaxies in a manner consistent with PG QSOs and lower luminosity Seyferts and LINERs, and (b) the X-ray emission from the AGN does not seem to be significantly suppressed, and thus these radio galaxies do not reside in Compton-thick environments. Indeed, several of the radio galaxies have measured column densities in the literature – the derived column densities from these X-ray observations are $\sim 10^{21-22} \text{ cm}^{-2}$ (Leighly et al. 1997; Sambruna et al. 1999; and Odea et al. 2000).

5.3. CO Luminosity and $L_{\text{IR}}/L'_{\text{CO}}$ versus Radio Power

Another issue relevant to the present sample of galaxies is whether the molecular gas properties are correlated with the radio output of the radio galaxies. I.e., if molecular gas fuels AGN activity, there may be a correlation between L'_{CO} and the energy emitted by these AGN at radio wavelengths. Figure 8a is a plot of L'_{CO} versus $L_{1.4\text{GHz}}$ of the sample of radio galaxies; comparative samples of infrared galaxies, PG QSOs, and ellipticals are also plotted. The infrared galaxy and PG QSO data are correlated, with higher L'_{CO} corresponding to higher $L_{1.4\text{GHz}}$. Such a correlation can be understood, for example, if a significant fraction of the 1.4 GHz emission is generated via star formation – the higher the molecular gas content, the higher the number of supernovae generating radio emission. The radio galaxies occupy a different location on this plot, having high $L_{1.4\text{GHz}}$ for their L'_{CO} relative to infrared galaxies and QSOs. It is also clear from the radio galaxy data that no obvious correlation exists between $L_{1.4\text{GHz}}$ and L'_{CO} . This result may simply illustrate the fact

that, if a correlation between the AGN radio output and molecular gas mass exists, it may only exist for the component of the molecular gas in the nuclear region (near the AGN), and not the global molecular gas mass measured by these observations.

Figure 8b is a plot of $L_{\text{IR}}/L'_{\text{CO}}$ versus $L_{1.4\text{GHz}}$. In terms of the distribution of infrared galaxies and QSO data, the plot is reminiscent of Figure 6b – $L_{\text{IR}}/L'_{\text{CO}}$ increases with increasing $L_{1.4\text{GHz}}$, and the QSOs and warm infrared galaxies reside primarily at high $L_{\text{IR}}/L'_{\text{CO}}$ and $L_{1.4\text{GHz}}$ relative to cool infrared galaxies. The radio galaxies occupy a different location on the plot, having high $L_{1.4\text{GHz}}$ for their $L_{\text{IR}}/L'_{\text{CO}}$, but no obvious correlation among the radio galaxy data exists. Thus, regardless of whether stars or AGN in the host galaxy of these radio galaxies are heating the dust, the fueling efficiency factor $L_{\text{IR}}/L'_{\text{CO}}$ is not correlated with the total radio output.

5.4. High Mass Star Formation

All but one of the radio galaxies detected as part of this survey have molecular gas masses in excess of $1 \times 10^9 M_{\odot}$, indicating that there are large fuel reservoirs for star formation and possibly AGN activity. The presence of molecular gas, in itself, is not evidence of active star formation. High mass star formation in the Milky Way occurs in the cores of giant molecular clouds (GMCs) where the molecular gas densities exceed $\sim 10^5 \text{ cm}^{-3}$.

Preliminary observations have been done of PKS 0502-10 and B2 0722+30 to provide additional information about the state of the molecular gas. The first observations are of the CO(2 \rightarrow 1) emission line; the $L'_{\text{CO}(2 \rightarrow 1)}/L'_{\text{CO}(1 \rightarrow 0)}$ ratios of PKS 0502-10 and B2 0722+30 are 0.6 and 0.7, respectively. Such low values of $L'_{\text{CO}(2 \rightarrow 1)}/L'_{\text{CO}(1 \rightarrow 0)}$ are suggestive of subthermally excited CO, i.e., low molecular gas temperatures and densities.

The second set of preliminary observations designed to probe the state of the gas in these radio galaxies are of the high density tracer HCN. HCN is seen in abundance when the molecular gas densities are on the order of 10^5 cm^{-3} , and thus is found in the cores of GMCs where massive star formation is commencing. Gao & Solomon (2004) have presented an HCN survey of infrared galaxies, and have calculated an average $L_{\text{IR}}/L'_{\text{HCN}}$ ratio of $\sim 970 \pm 600$. The HCN(1 \rightarrow 0) observations of two radio galaxies yielded only upper

limits, translating into $L_{\text{IR}}/L'_{\text{HCN}}$ lower limits of ~ 550 and 3700 for PKS 0502-10 and B2 0722+30, respectively. Thus, while the $L_{\text{IR}}/L'_{\text{HCN}}$ of PKS 0502-10 does not provide a useful constraint, the high $L_{\text{IR}}/L'_{\text{HCN}}$ of B2 0722-30 is suggestive of either highly efficient massive star formation or significant heating of dust by the AGN.

5.5. Are Fanaroff-Riley II Radio Galaxies Relatively Molecular Gas Poor?

One of the goals of this survey was to obtain detections of CO emission from radio galaxies of all morphological types. This survey yielded a CO detection in only one Fanaroff-Riley II (edge-brightened radio morphology: Fanaroff & Riley 1974) radio galaxy, 3C 293. However, in terms of its radio properties, 3C 293 is not a representative F-R II. The galaxy has a low radio power ($L_{1.4\text{GHz}} \sim 2 \times 10^{25} \text{ W m}^{-2} \text{ Hz}^{-1}$) relative to the bulk of F-R II radio galaxies. In addition, 3C 293 has a complex steep spectrum core which shows evidence of a previous radio outburst (Akujor et al. 1996).

The low CO detection rate of F-R II galaxies ($\sim 8\%$) relative to F-R I and compact radio source galaxies ($\sim 35\%$) may be a simple consequence of larger distances of F-R II galaxies, on average, relative to lower radio power radio galaxies in the sample. This explanation is unlikely; Figure 6a shows the L'_{CO} of the detected radio galaxies and the L'_{CO} upper limits of the undetected galaxies. The upper limits of all of the non-detected F-R II galaxies are below $2.5 \times 10^9 \text{ K km s}^{-1} \text{ pc}^2$, and three out of seven (excluding B2 1318+34) of the CO-detected F-R I and compact radio galaxies are above this line. Thus, though the F-R II galaxies comprise 36% of the sample, there are no additional F-R II galaxies in the sample with molecular gas masses comparable to either 3C 293, or the most gas-rich F-R I and radio compact galaxies (PKS 0502-10, TXS 1506+345, and PKS 1345+12) in the sample. This result, of course, relies on the assumption that F-R II radio galaxies have CO emission line widths of $\sim 500 \text{ km s}^{-1}$; if the line widths are sufficiently broad, then the limited velocity bandwidth (i.e., $\sim 1400 \text{ km s}^{-1}$ at 3mm) available with single-dish telescopes such as the 12m Telescope would make the CO detections difficult.

The present CO survey has focussed on a sample of IRAS-detected radio galaxies using a

fairly moderate size single-dish millimeter telescope. The results presented here can be improved upon in the following ways: *(i)* CO surveys of larger samples of ISO and Spitzer Space Telescope-detected radio galaxies using larger single-dish millimeter-wave telescopes or interferometers. *(ii)* Volume-limited CO surveys of radio galaxies (and QSOs) similar to those initiated by Lim et al. (1999) and Scoville et al. (2003). Such surveys will provide a more complete view of the molecular gas properties of radio (and UV-selected) AGN. *(iii)* Interferometric observations of the CO-detected radio galaxies to measure the extent, surface density, and kinematics of the molecular gas relative to the stellar population and the ionized/neutral gas (Inoue et al. 1996; Evans et al. 1999a,b; Okuda et al. 2005; Evans et al. 2005a). Finally, continued investigations of star formation in radio galaxies using diagnostics at multiple wavelengths will provide a more complete picture of the putative starburst-AGN connection. Recent optical spectroscopy of three of the galaxies in the sample (3C 293, 3C 305, and PKS 1345+12: Tadhunter et al. 2005) have provided encouraging results.

6. SUMMARY

The survey presented here is a follow-up to the Mazzarella et al. (1993) study of IRAS-detected radio galaxies, which yielded new CO detections in three radio galaxies. The survey has increased the number of low-redshift radio galaxies observed in the prior survey by a factor of four. The following conclusions have been reached:

(1) Three additional radio galaxies (3C 31, PKS 0502-10, 3C 293) have been detected in CO($1 \rightarrow 0$), yielding a total of 9 detections out of 33 radio galaxies. The CO detections translate into molecular gas masses of $0.4 - 7 \times 10^9 M_{\odot}$, with 3σ upper limits for nondetections in the range of $< 4 \times 10^8 M_{\odot}$ for a $z \sim 0.02$ galaxy to $< 3.3 \times 10^9 M_{\odot}$ for a $z \sim 0.1$ galaxy ($\alpha = 1.5 M_{\odot} [\text{K km s}^{-1} \text{ pc}^2]^{-1}$). Thus, the upper limits of the more distant members of the sample do not rule out molecular gas mass as high as that of the Milky Way ($\sim 3 \times 10^9 M_{\odot}$).

(2) Many of the CO lines have double-peaked profiles, which is indicative of either CO absorption towards the AGN, or CO distributed in a molecular ring.

(3) The CO line widths are extremely broad. The average velocity dispersion of the CO-

detected radio galaxies is $\Delta v_{\text{FWHM}} = 500 \pm 130 \text{ km s}^{-1}$, which exceeds the average line width of both ultraluminous infrared galaxies ($= 300 \pm 90 \text{ km s}^{-1}$) and PG QSOs ($= 260 \pm 160 \text{ km s}^{-1}$). This is an indication that the CO-luminous radio galaxies are massive.

(4) With the exception of the edge-on spiral galaxy B2 0722+30, optical images show the molecular gas-rich radio galaxies to have close companions and/or tidal features consistent with those of infrared-luminous interacting and merging galaxy systems.

(5) Most of the radio galaxies have $L_{\text{IR}}/L'_{\text{CO}}$ similar to GMCs. Exceptions to this include *(i)* PKS 1345+12, which has a $L_{\text{IR}}/L'_{\text{CO}} (\sim 370)$ comparable to the PG QSOs, likely an indication of highly efficient massive star production or of significant dust heating by the AGN, and *(ii)* 3C 31, PKS 0502-10, and 3C 293, which have low $L_{\text{IR}}/L'_{\text{CO}}$ (< 30) consistent with the global $L_{\text{IR}}/L'_{\text{CO}}$ of spiral galaxies.

(6) All of the radio galaxies have measured values of $L_{\text{X}}/L_{\text{FIR}}$ significantly higher than the average for HII-region like galaxies. Thus, the AGN is the major contributor to the X-ray emission, and the AGN do not reside in Compton-thick environments.

(7) No correlation exists between L'_{CO} or $L_{\text{IR}}/L'_{\text{CO}}$ and $L_{1.4\text{GHz}}$ of the radio galaxies.

(8) Only one F-R II radio galaxy (3C 293) was detected, yielding an 8% CO detection rate for F-R II galaxies. By comparison, $\sim 35\%$ of the F-R I and compact radio source galaxies were detected. The L'_{CO} upper limits of the undetected F-R II galaxies are sufficiently small to support the conclusion that either low-redshift F-R II galaxies are gas-poor compared with F-R I and radio compact galaxies, or that the CO line widths of the undetected F-R II galaxies are broad enough to make their detection difficult with a single-dish telescope.

We thank the telescope operators and staff of the NRAO 12m and IRAM 30 telescopes for their support both during and after the observations were obtained, and the anonymous referee for many useful comments and suggestions. ASE also thanks N. Trentham for useful discussions and assistance. ASE was supported by NSF grant AST 02-06262 and the 2002 NASA/ASEE Faculty Fellowship. DTF, JMM, and JAS were supported by the Jet Propulsion Laboratory, California Insti-

tute of Technology, under contract with NASA. D.B.S. gratefully acknowledges the hospitality of the Max-Plank Institut fur Extraterrestrische Physik and the Alexander von Humboldt Stiftung for a Humboldt senior award, and partial financial support from NASA grant GO-8190.01-97A. This research has made use of the NASA/IPAC Extragalactic Database (NED) which is operated by the Jet Propulsion Laboratory, California Institute of Technology, under contract with the National Aeronautics and Space Administration.

REFERENCES

- Allen, M. G. et al. 2002, *ApJS*, 139, 411
- Barvainis, R., Alloin, D., & Antonucci, R. 1989, *ApJ*, 337, 69
- Barvainis, R., Lonsdale, C. & Antonucci, R. 1996, *AJ*, 111, 1431
- Baum, S. A., Heckman, T. M., & van Breugel, W. 1992, *ApJ*, 389, 208
- Becker, R. H., White, R. L. & Helfand, D. J. 1995, *ApJ*, 450, 559
- Boller, T., Gallo, L., Lutz, D., & Sturm, E. 2002, *MNRAS*, 336, 1143
- Bushouse, H. A. & Stanford, S. A. 1992, *ApJS*, 79, 213
- Condon, J. J. 1992, *ARA&A*, 30, 575
- Condon, J. J., Cotton, W. D., Greisen, E. W., Yin, Q. F., Perley, R. A., Taylor, G. B., & Broderick, J. J. 1998, *AJ*, 115, 1693
- Condon, J., Helou, G., Sanders, D. B., Soifer, B. T. 1990, *ApJS*, 73, 359
- Condon, J., Huang, Yin, & Thuan 1991, *ApJ*, 378, 65
- Churazov, E., Forman, W., Jones, C. Boehringer, H. 2003, *ApJ*, 590, 225
- Di Matteo, T., Allen, S. W., Fabian, A. C., Wilson, A. S., & Young, A. J. 2003, *ApJ*, 582, 113
- Della Ceca, R. et al. 2002, *ApJ*, 581, 9
- Devereux, N. A. & Young, J. S. 1990, *ApJ*, 359, 42
- Downes, D. & Solomon, P. M. 1998, *ApJ*, 507, 615
- Elfhag, T., Booth, R. S., Hoglund, B., Johansson, L. E. B., & Sandqvist, Aa. 1996, *A&AS*, 115, 439
- Evans, A. S. 1996, PhD Thesis, University of Hawaii
- Evans, A. S. 1998, in Highly Redshifted Radio Lines, eds. C. Carilli, S. J. E. Radford, K. Menten, & G. Langston, 156, 74
- Evans, A. S., Frayer, D. T., Surace, J. A., & Sanders, D. B. 2001, *AJ*, 121, 3286
- Evans, A. S., Kim, D.-C., Mazzarella, J. M., Scoville, N. Z., & Sanders, D. B. 1999b, *ApJ*, 520, L107
- Evans, A. S., Mazzarella, J. M., Surace, J. A., Frayer, D. T., Vavilkin, T., & Sanders, D. B. 2005a, in preparation
- Evans, A. S., Mazzarella, J. M., Surace, J. A., & Sanders, D. B. 2002, *ApJ*, 580, 749
- Evans, A. S., Sanders, D. B., Mazzarella, J. M., Solomon, P. M., Downes, D., Kramer, C., & Radford, S. J. E. 1996, *ApJ*, 457, 658
- Evans, A. S., Sanders, D. B., Surace, J. A., & Mazzarella, J. M. 1999a, *ApJ*, 511, 730
- Evans, A. S., Solomon, P. M., Tacconi, L., Downes, D., & Vavilkin, T. 2005b, in preparation
- Franceschini, A. et al. 2003, *MNRAS*, 343, 1181
- Fanaroff, B. L., & Riley, F. M. 1974, *MNRAS*, 167, 31P
- Gao, Y. & Solomon, P. M. 2004, *ApJS*, 152, 63
- Golombek, D., Miley, G. K.. & Neugebauer, G. 1988, *AJ*, 95, 26
- Grimm, H.-J., Gilfanov, M. & Sunyaev, R. 2003, *MNRAS*, 339, 793
- Güsten, R., Serabyn, E., Kasemann, C., Schinckel, A., Schneider, G., Schulz, A., & Young, K. 1993, *ApJ*, 402, 537
- Haas, M. et al. 2003, *A&A*, 402, 87
- Haas, M. et al. 2004, *A&A*, 424, 531
- Heckman, T. M. et al. 1986, *ApJ*, 311, 526
- Inoue, M. Y., Kamenou, S., Kawabe, R., & Inoue, M. 1996, *AJ*, 111, 1852
- Iwasawa, K., Comastri, A. 1998, *MNRAS*, 297, 1219
- Kim, D.-C., Veilleux, S., & Sanders, D. B. 2003, *ApJS*, 147, 221
- Knapp, G. R. & Rupen, M. P. 1996, *ApJ*, 460, 271
- Lazareff, B., Castets, A., Kim, D.-W., & Jura, M. 1989, *ApJ*, 336, L13
- Leighly, K. M. et al. 1997, *ApJ*, 483, 767
- Lim, J., Leon, S., Combes, F., Trung, D.-V. 2000, *ApJ*, 545, L93
- Lonsdale, C. J., Smith, H. E., Lonsdale, C. J. 1995, *ApJ*, 438, 632
- Magorrian, J. et al. 1998, *AJ*, 115, 2285
- Martel, A. R. 1999, *ApJS*, 122, 81
- Mazzarella, J. M., Graham, J. R., Sanders, D. B., & Djorgovski, S. 1993, *ApJ*, 409, 170
- McLeod, K. K., & Rieke, G. H. 1994, *ApJ*, 431, 137
- McNamara, B. R. et al. 2000, *ApJ*, 534, L135
- Meisenheimer, K., Haas, M., Müller, S. A. H., Chini, R., Klaas, U., Lemke, D. 2001, *A&A*, 372, 719
- Mirabel, I. F., Sanders, D. B., & Kazès, I. 1989, *ApJ*, 340, L9
- Moshir, M. et al. 1990, Infrared Astronomical Satellite Catalogs, The Faint Source Catalog, Version 2.0
- O'Dea, C. P., De Vries, W. H., Worral, D. M., Baum, S. A., & Koekemoer, A. 2000, *AJ*, 119, 478
- Okuda, T., Kohno, K., Iguchi, S., & Nakanishi, K. 2005, *ApJ*, 620, 673
- Phillips, T. G. et al. 1987, *ApJ*, 322, 73
- Radford, S. J. E., Solomon, P. M., & Downes, D. 1991, *ApJ*, 368, L15
- Ranalli, P., Comastri, A. & Setti, G. 2003, *A&A*, 399, 39
- Reuter, H.-P., Pohl, M., Lesch, H., Sievers, A. W. 1993, *A&A*, 277, 21
- Sambruna, R. M., Eracleous, M. & Mushotzky, R. F. 1999, *ApJ*, 526, 60
- Sandage, A. 1966, *ApJ*, 145, 1
- Sanders, D. B. & Mirabel, I. F. 1996, *ARA&A*, 34, 749
- Sanders, D. B., Scoville, N. Z., & Soifer, B. T. 1988c, *ApJ*, 335, 1
- Sanders, D. B., Scoville, N. Z., & Soifer, B.T. 1991, *ApJ*, 370, 158
- Sanders, D.B., Soifer, B.T., Elias, J.H., Madore, B.F., Matthews, K., Neugebauer, G., & Scoville, N.Z. 1988a, *ApJ*, 325, 74
- Sanders, D.B., Soifer, B.T., Elias, J.H., Neugebauer, G. & Matthews, K. 1988b, *ApJ*, 328, L35
- Schmidt, M. & Green, R. F. 1983, *ApJ*, 269, 352
- Scoville, N. Z. et al. 2000, *AJ*, 119, 991
- Scoville, N. Z., Frayer, D. T., Schinnerer, E., & Christopher, M. 2003, *ApJ*, 585, L105
- Scoville, N. Z. & Sanders, D. B. 1987, in Interstellar Processes, ed. D. Hollenbach & H. Thronson (Dordrecht: Reidel), 21
- Smith, E. P. & Heckman, T. M. 1989a, *ApJS*, 69, 365
- Smith, E. P. & Heckman, T. M. 1989b, *ApJ*, 341, 658
- Solomon, P. M., Downes, D., & Radford, S. J. E. 1992, *ApJ*, 398, L29
- Solomon, P. M., Downes, D., Radford, S. J. E. & Barrett, J. W. 1997, *ApJ*, 478, 144
- Stockton, A. & MacKenty, J. W. 1983, *Nature*, 305, 678
- Strong, A. W. et al. 1988, *A&A*, 207, 1
- Surace, J. A., Sanders, D. B., & Evans, A. S. 2001, *AJ*, 122, 2791
- Tadhunter, C., Robinson, T. G., Gonzalez, R. M., Wills, K., Morganti, R. 2005, *MNRAS*, 356, 480
- Terashima, Y., Iyomoto, N., Ho, L. C. & Ptak, A. F. 2002, *ApJS*, 139, 1
- Trentham, N., Iwasawa, K., Ramirez-Ruiz, E., Evans, A. S., & Sanders, D. B. 2005, in preparation
- Veilleux, S., Sanders, D. B., & Kim, D.-C. 1997, *ApJ*, 484, 92
- Veilleux, S., Kim, D.-C., & Sanders, D. B. 1999, *ApJ*, 522, 113
- Veilleux, S., Kim, D.-C., & Sanders, D. B. 1999, *ApJ*, 522, 139
- Vignati, P. et al. 1999, *A&A*, 349, 57

- Wainscoat, R. J. 1996, University of Hawaii Telescopes at Telescopes at Mauna Kea Observatory - User Manual, University of Hawaii
- White, R. L. & Becker, R. H. 1992, *ApJS*, 79, 331
Wiklind, T. & Combes, D. 1997, *A&A*, 324, 51
Young, J. S. & Scoville, N. Z. 1991, *ARA&A*, 29, 581

Figure Captions

Figure 1. (a) NRAO 12m and IRAM 30m CO(1→0) spectrum of 31 of the 33 radio galaxies in the survey. The intensity scale is in units of main beam brightness temperature. A linear baseline has been subtracted from each spectrum; the baseline subtraction is performed outside of the velocity range of emission lines when they are present. With the exception of PKS 0502-10, the zero velocity corresponds to the redshift of the radio galaxy listed in Table 1. The zero velocity redshift of PKS 0502-10 is 0.0396. (b) IRAM 30m CO(1→0) spectrum of PKS 1345+12. The spectrum confirm the general features of the 12m spectrum of Figure 1a, but with significantly higher signal-to-noise.

Figure 2. JCMT 15m and IRAM 30m telescope CO(2 → 1) spectra of PKS 0502-10, B2 0722+30, and Cygnus A. The intensity scale is in units of main beam brightness temperature (IRAM) and antenna temperature corrected for aperture losses (JCMT). A linear baseline has been subtracted from each spectrum; the baseline subtraction is performed outside of the velocity range of emission lines when they are present. Zero velocity corresponds to the redshift of the radio galaxy listed in Table 3.

Figure 3. IRAM 30m HCN(1 → 0) spectra of PKS 0502-10 and B2 0722+30. The intensity scale is in units of main beam brightness temperature. A linear baseline has been subtracted from each spectrum; the baseline subtraction is performed outside of the velocity range where the HCN emission line is expected to be. Zero velocity corresponds to the redshift of the radio galaxy listed in Table 3.

Figure 4. False-color U' , B , and I -band images of seven of the radio galaxies detected in CO(1 → 0). The U , B , and I -band data are displayed as blue, green, and red, respectively. North is up, and east is to the left.

Figure 5. The ratio of 1.4 GHz to infrared luminosity versus the infrared luminosity of infrared luminous radio galaxies, a sample of infrared galaxies, PG QSOs and elliptical galaxies detected in CO. References for the infrared data are as follows: infrared galaxies, Mazzarella et al. (1993); PG QSOs, Sanders et al. (1989) and Haas et al. (2003); elliptical galaxies (Moshir et al. 1990). References for the 1.4 GHz data are as follows: infrared galaxies, Condon et al. (1990, 1991, 1992); elliptical galaxies (White & Becker 1992; Becker et al. 1995; Condon et al. 1998); radio galaxies (White & Becker 1992; Becker et al. 1995); PG QSOs (White & Becker 1992; Barvainis, Lonsdale, & Antonucci 1996; Condon et al. 1998).

Figure 6. (a) CO vs. infrared luminosity plot of infrared luminous radio galaxies, a sample of infrared galaxies, PG QSOs and elliptical galaxies detected in CO. References for CO data are as follows: infrared galaxies, Mazzarella et al. (1993); PG QSOs, Sanders et al. (1988c), Barvainis et al. (1989), Evans et al. (2001), and Scoville et al. (2003); elliptical galaxies: Wiklind & Combes (1997). (b) the ratio of infrared to CO luminosity vs. infrared luminosity for the same sample of galaxies as in 6(a). In both Figures, the galaxy B2 1318+34 is denoted by an unfilled triangle.

Figure 7. (a) Hard (2-10 keV) X-ray luminosity vs. far-infrared luminosity plot of the infrared luminous radio galaxies and a comparison sample of infrared galaxies, PG QSOs, and less luminous galaxies classified as HII region-like galaxies, Seyferts, and LINERs. The far-infrared luminosities have been calculated using data in NED. The radio galaxies in the Figure are NGC 315, 3C 84, 3C 111, 3C 120, PKS 0634-20, Hydra A, M87, PKS 1345+12, 3C 293, 3C 321, NGC 6251, 3C 390.3, and 3C 405. References for the X-ray data are as follows: HII, Seyferts, and LINERs, Terashima et al. (2002) and Grimm et al. (2003); infrared luminous galaxies, Iwasawa & Comastri (1998), Boller (2002), Dalla Ceca (2002), Franceschini et al. (2003), and Sanders et al. (2005); radio galaxies, Churazov et al. (2003); Di Matteo et al. (2003); Leighly et al. (1997); McNamara et al. (2000); Odea et al. (2000); and Sambruna et al. (1999). The X-ray luminosity of 3C 293 ($L_X \sim 3 \times 10^{42}$ erg s $^{-1}$) was calculated by us from archival ASCA data. (b) Ratio of the X-ray to far-infrared luminosity versus the far-infrared luminosity for the same sample of galaxies as in Figure 7(a). In both (a) and (b), radio galaxies and PG QSOs with CO detections are encircled. Adapted from Trentham et al. (2005).

Figure 8. (a) The CO luminosity vs. the radio power of the infrared luminous radio galaxies and a comparison sample of infrared galaxies, PG QSOs, and elliptical galaxies. (b) $L_{\text{IR}}/L'_{\text{CO}}$ vs. the radio power for the same sample of galaxies plotted in 8a. In both Figures, the galaxy B2 1318+34 is denoted

by an unfilled triangle.

TABLE 1
SOURCE LIST

Source	Coordinates (J2000.0)			z	FR	$f_{60\mu\text{m}}$ (mJy)	$f_{100\mu\text{m}}$ (mJy)	L_{IR}^{a} (L_{\odot})	$L_{\text{FIR}}^{\text{a}}$ (L_{\odot})	$P_{1.5\text{GHz}}$ (W m $^{-2}$ Hz $^{-1}$)
NGC 315	00h57m48.85s	+30d21m08.63s	0.0165	I	368	460	7.2×10^9	2.3×10^9	1.6×10^{24}	
3C 31	01h07m24.98s	+32d24m44.77s	0.0167	I	435	1675	7.4×10^9	4.7×10^9	2.5×10^{24}	
4C 31.04	01h19m35.00s	+32d10m50.03s	0.0590	C	150	524	3.7×10^{10}	1.9×10^{10}	1.7×10^{25}	
NGC 741	01h56m21.05s	+05d37m44.17s	0.0185	C	214	777	7.0×10^9	2.7×10^9	6.0×10^{23}	
3C 84	03h19m48.09s	+41d30m42.47s	0.0176	I	7427	8267	1.6×10^{11}	5.1×10^{10}	7.3×10^{24}	
3C 88	03h27m54.17s	+02d33m41.85s	0.0302	II	180	816	1.7×10^{10}	7.0×10^9	8.5×10^{24}	
3C 111	04h18m21.07s	+38d01m32.59s	0.0485	II	321	<2250	9.0×10^{10}	2.8×10^{10}	6.5×10^{25}	
3C 120	04h33m11.09s	+05d21m16.03s	0.0331	I	1383	1937	1.2×10^{11}	3.6×10^{10}	9.0×10^{24}	
PKS 0502-10	05h04m52.99s	-10d14m52.18s	0.0410	?	688	1370	6.1×10^{10}	3.0×10^{10}	4.6×10^{24}	
PKS 0634-20	06h36m32.24s	-20d34m52.92s	0.0544	II	484	1150	9.5×10^{10}	4.3×10^{10}	3.3×10^{25}	
B2 0648+27	06h42m02.82s	+27d28m21.69s	0.0414	C	2633	1529	2.2×10^{11}	8.7×10^{10}	4.9×10^{23}	
B2 0722+30	07h25m37.35s	+29d57m14.71s	0.0188	I	3108	4999	5.2×10^{10}	2.8×10^{10}	8.2×10^{22}	
4C 29.30	08h40m02.44s	+29d49m02.87s	0.0650	I	472	595	1.1×10^{11}	4.7×10^{10}	3.3×10^{23}	
Hydra A	09h18m05.69s	-12d05m45.45s	0.0538	I	155	416	2.8×10^{10}	1.4×10^{10}	2.5×10^{26}	
3C272.1	12h25m03.78s	+12d53m13.1s	0.0035	I	556	1024	5.6×10^8	1.8×10^8	1.0×10^{23}	
M 87	12h30m49.35s	+12d23m28.06s	0.0047	I	546	559	1.1×10^9	2.6×10^8	7.2×10^{24}	
B2 1318+34	13h20m35.20s	+34d08m13.56s	0.0233	I	16070	20682	3.4×10^{11}	2.0×10^{11}	8.9×10^{22}	
3C 285	13h21m17.78s	+42d35m14.23s	0.0789	II	253	637	1.8×10^{11}	5.0×10^{10}	2.6×10^{25}	
PKS 1345+12	13h47m33.38s	+12d17m24.18s	0.1224	C	2098	1738	1.5×10^{12}	6.7×10^{11}	1.5×10^{26}	
3C 293	13h52m17.86s	+31d26m46.67s	0.0450	II	233	621	2.9×10^{10}	1.5×10^{10}	1.7×10^{25}	
OQ 208	14h07m00.39s	+28d27m14.73s	0.0768	C	753	1029	4.1×10^{11}	1.1×10^{11}	8.3×10^{24}	
3C 305	14h49m21.46s	+63d16m16.14s	0.0410	I	298	450	2.4×10^{10}	1.2×10^{10}	9.4×10^{24}	
TXS 1506+345	15h08m05.64s	+34d23m22.75s	0.0449	I	2647	3956	2.3×10^{11}	1.3×10^{11}	4.5×10^{23}	
PKS B1518+045	15h21m22.61s	+04d20m29.21s	0.0513	?	<120	968	4.6×10^{10}	1.8×10^{10}	2.1×10^{25}	
3C 321	15h31m43.45s	+24d04m18.70s	0.0960	II	1067	961	5.0×10^{11}	2.1×10^{11}	6.2×10^{25}	
3C 327	16h02m27.39s	+01d57m55.70s	0.1048	II	670	371	4.1×10^{11}	1.4×10^{11}	1.9×10^{26}	
NGC 6251	16h32m31.97s	+82d32m16.46s	0.0249	I	188	600	5.7×10^9	2.7×10^9	2.6×10^{24}	
B2 1707+34	17h09m38.37s	+34d25m53.76s	0.0808	II	464	841	2.0×10^{11}	8.2×10^{10}	8.4×10^{24}	
3C 390.3	18h42m08.92s	+79d46m17.27s	0.0561	II	250	340	1.3×10^{11}	1.9×10^{10}	7.2×10^{25}	
3C 402	19h41m46.00s	+50d35m44.86s	0.0254	II	257	1052	1.1×10^{10}	6.6×10^9	3.1×10^{24}	
3C 403	19h52m15.36s	+02d30m28.14s	0.0590	II	441	<500	1.5×10^{11}	3.0×10^{10}	3.9×10^{25}	
3C 405	19h59m28.51s	+40d44m01.70s	0.0556	II	2847	<1800	4.0×10^{11}	1.6×10^{11}	9.4×10^{27}	
3C 433	21h23m44.53s	+25d04m09.99s	0.1016	I	299	<1200	2.9×10^{11}	8.8×10^{10}	2.3×10^{24}	

^aBoth L_{IR} and L_{FIR} are calculated using the prescription in Sanders & Mirabel (1996). In cases where one or more IRAS flux densities have only upper limit values, L_{IR} and L_{FIR} are calculated by setting the flux density value equal to the upper limit value and by setting the flux density value equal to zero, then taking the average of these two determinations.

REFERENCES.—Fanaroff-Riley classifications: Golombek et al. 1988; Baum, Heckman, & van Breugel 1992; <http://www.jb.man.ac.uk/atlas/>. Flux Densities: Golombek et al. 1988; Redshifts: Golombek et al. 1988; Mirabel et al. 1989; Mazzarella et al. 1993.

TABLE 2
JOURNAL OF OBSERVATIONS

Source	Site	Transition	Date (mmm-yy)	Time (hr)	T _{sys} (K)
NGC 315	12m	CO(1→0)	Oct-97	3.0	420
3C 31	12m	CO(1→0)	Jan-96	17.4	272
	12m	CO(1→0)	Jun-97	18.4	333
	12m	CO(1→0)	Oct-97	4.6	273
4C 31.04	12m	CO(1→0)	Jan-96	29.6	199
NGC 741	12m	CO(1→0)	Jun-97	12.4	371
3C 84	12m	CO(1→0)	Jun-97	4.8	318
3C 88	12m	CO(1→0)	Oct-97	7.2	248
3C 111	12m	CO(1→0)	Sep-95	10.2	260
3C 120	12m	CO(1→0)	Oct-97	19.6	259
PKS 0502-10	12m	CO(1→0)	Sep-95	14.8	369
	12m	CO(1→0)	Jan-96	9.4	256
	15m	CO(2→1)	Sep-95	4.0	411
	30m	HCN(1→0)	Dec-03	1.8	120
PKS 0634-20	12m	CO(1→0)	Jun-97	5.2	372
	12m	CO(1→0)	Oct-97	12.6	256
B2 0648+27	12m	CO(1→0)	Sep-95	24.6	319
	12m	CO(1→0)	Jan-96	2.6	237
B2 0722+30	12m	CO(1→0)	Oct-97	6.6	299
	15m	CO(2→1)	Sep-95	1.8	469
	30m	HCN(1→0)	Dec-03	1.8	83
4C 29.30	12m	CO(1→0)	Jan-96	12.2	220
	12m	CO(1→0)	Jun-97	30.8	232
	12m	CO(1→0)	Oct-97	8.2	196
Hydra A	12m	CO(1→0)	Jun-97	5.2	288
	12m	CO(1→0)	Oct-97	9.4	224
M 87	12m	CO(1→0)	Dec-92	21.9	368
B2 1318+34	12m	CO(1→0)	Oct-97	1.8	256
3C 285	12m	CO(1→0)	Jan-96	49.6	210
PKS 1345+12	12m	CO(1→0)	Jun-97	30.1	256
	12m	CO(1→0)	Jun-00	4.3	200
3C 293	12m	CO(1→0)	Jan-96	17.6	240
OQ 208	12m	CO(1→0)	Sep-95	12.8	261
3C 305	12m	CO(1→0)	Oct-97	16.0	261
TXS 1506+345	12m	CO(1→0)	Oct-97	8.4	211
PKS B1518+045	12m	CO(1→0)	Jun-97	9.4	269
3C 321	12m	CO(1→0)	Sep-95	23.6	276
	12m	CO(1→0)	Jun-97	16.4	249
3C 327	12m	CO(1→0)	Oct-97	5.6	321
	12m	CO(1→0)	Jun-00	16.2	205
B2 1707+34	12m	CO(1→0)	Jun-97	13.0	252
	12m	CO(1→0)	Oct-97	12.0	208
3C 390.3	12m	CO(1→0)	Jun-97	16.4	356
	12m	CO(1→0)	Oct-97	5.2	464
3C 402	12m	CO(1→0)	Oct-97	6.0	248

TABLE 2—Continued

Source	Site	Transition	Date (mmm-yy)	Time (hr)	T _{sys} (K)
3C 403	12m	CO(1→0)	Jun-97	11.4	254
3C 405	30m	CO(1→0)	Nov-95	5.9	186
	30m	CO(2→1)	Nov-95	3.3	321
3C 433	12m	CO(1→0)	Jan-96	11.6	200
	12m	CO(1→0)	Oct-97	13.0	179

TABLE 3
MOLECULAR GAS EMISSION LINE PROPERTIES

Source	D _L ^a (Mpc)	line	Site	z _{CO}	Δv _{FWHM} (km s ⁻¹)	T _{mb} Δv ^b (K km s ⁻¹)	S _{line} Δv (Jy km s ⁻¹)	L _{line} (K km s ⁻¹ pc ²)	M(H ₂) ^c (M _⊙)
NGC 315	66	CO(1→0)	12m	<0.91	<23.0	<2.4×10 ⁸	<3.6×10 ⁸
3C 31	67	CO(1→0)	12m	0.0169	450	1.1±0.08	27±2	2.9×10 ⁸	4.3×10 ⁸
4C 31.04	239	CO(1→0)	12m	<0.21	<5.2	<6.7×10 ⁸	<1.0×10 ⁹
NGC 741	74	CO(1→0)	12m	<0.39	<9.8	<1.3×10 ⁸	<1.9×10 ⁸
3C 84	71	CO(1→0)	12m	0.0176	200	4.1±0.05	104±1	1.2×10 ⁹	1.8×10 ⁹
3C 88	122	CO(1→0)	12m	<0.41	<10.4	<3.6×10 ⁸	<5.4×10 ⁸
3C 111	196	CO(1→0)	12m	<0.34	<8.5	<7.5×10 ⁸	<1.1×10 ⁹
3C 120	133	CO(1→0)	12m	0.0331	550	1.1±0.1	28±2	1.2×10 ⁹	1.7×10 ⁹
PKS 0502-10	160	CO(1→0)	12m	0.0398	550	1.8±0.09	45±2	2.7×10 ⁹	4.0×10 ⁹
...	...	CO(2→1)	15m		550	4.7±0.3	110±7	1.6×10 ⁹	...
...	...	HCN(1→0)	30m		550	<0.33	<2.0	<1.1×10 ⁸	...
PKS 0634-20	220	CO(1→0)	12m	<0.38	<9.6	<1.0×10 ⁹	<1.6×10 ⁹
B2 0648+27	167	CO(1→0)	12m	<0.26	<6.6	<4.3×10 ⁸	<6.4×10 ⁸
B2 0722+30	76	CO(1→0)	12m	0.0188	450	2.3±0.2	58±4	7.9×10 ⁸	1.2×10 ⁹
...	...	CO(2→1)	15m		450	6.8±0.2	160±5	5.4×10 ⁸	...
...	...	HCN(1→0)	30m		450	<0.18	<1.1	<1.4×10 ⁷	...
4C 29.30	264	CO(1→0)	12m	<0.18	<4.5	<7.1×10 ⁸	<1.1×10 ⁹
Hydra A	218	CO(1→0)	12m	<0.25	<6.4	<6.9×10 ⁸	<1.0×10 ⁹
M 87	19	CO(1→0)	12m	<0.46	<11.7	<1.0×10 ⁷	<1.5×10 ⁷
B2 1318+34	94	CO(1→0)	12m	0.0233	400	7.0±0.3	177±7	3.6×10 ⁹	5.5×10 ⁹
3C 285	322	CO(1→0)	12m	<0.20	<4.9	<1.1×10 ⁹	<1.7×10 ⁹
PKS 1345+12	503	CO(1→0)	12m	0.1220	250	0.24±0.06	6.0±1.6	3.3×10 ⁹	4.9×10 ⁹
PKS 1345+12	503	CO(1→0)	30m		400	1.6±0.08	8.0±0.4	4.3×10 ⁹	6.5×10 ⁹
3C 293	182	CO(1→0)	12m	0.0448	700	2.2±0.09	56±2	4.3×10 ⁹	6.4×10 ⁹
OQ 208	313	CO(1→0)	12m	<0.31	<7.9	<1.7×10 ⁹	<2.6×10 ⁹
3C 305	166	CO(1→0)	12m	<0.34	<8.6	<5.4×10 ⁸	<8.2×10 ⁸
TXS 1506+345	181	CO(1→0)	12m	0.0449	550	2.5±0.09	63±2	4.8×10 ⁹	7.1×10 ⁹
PKS B1518+045	208	CO(1→0)	12m	<0.45	<11.3	<1.1×10 ⁹	<1.7×10 ⁹
3C 321	393	CO(1→0)	12m	<0.19	<4.7	<1.6×10 ⁹	<2.4×10 ⁹
3C 327	429	CO(1→0)	12m	<0.22	<5.4	<2.2×10 ⁹	<3.3×10 ⁹
B2 1707+34	329	CO(1→0)	12m	<0.19	<4.9	<1.2×10 ⁹	<1.8×10 ⁹
3C 390.3	227	CO(1→0)	12m	<0.41	<10.3	<1.2×10 ⁹	<1.8×10 ⁹
3C 402	102	CO(1→0)	12m	<0.41	<10.3	<2.5×10 ⁸	<3.8×10 ⁸
3C 403	239	CO(1→0)	12m	<0.38	<9.5	<1.2×10 ⁹	<1.9×10 ⁹
3C 405	225	CO(1→0)	30m	<0.37	<1.9	<2.1×10 ⁸	<3.2×10 ⁸
3C 433	416	CO(1→0)	12m	<0.16	<3.9	<1.5×10 ⁹	<2.2×10 ⁹

^aLuminosity Distance, calculated assuming $H_0 = 75 \text{ km s}^{-1} \text{ Mpc}^{-1}$, $q_0 = 0.5$, and $\Lambda = 0$.^bFor all radio galaxies with CO(1→0) non-detections, $T_{\text{mb}}\Delta v = 3T_{\text{mb}}(\text{rms})\Delta v_{\text{FWHM}}$, where $T_{\text{mb}}(\text{rms})$ is the root-mean-squared main-beam temperature and $\Delta v_{\text{FWHM}} = 500 \text{ km s}^{-1}$.^cCalculated assuming $\alpha = 1.5M_{\odot} [\text{K km s}^{-1} \text{ pc}^2]^{-1}$.

TABLE 4
ESTIMATION OF M_{dust} , M_{dyn} , AND COLUMN DENSITIES

Source	T_{dust} (K)	M_{dust} (M_{\odot})	$M(\text{H}_2)/M_{\text{dust}}$	R_{CO} (pc)	M_{dyn} (M_{\odot})	$M(\text{H}_2)/M_{\text{dyn}}$	Column Density (cm^{-2})
3C 31	33	2.7×10^6	160	75	4.2×10^9	0.10	1.6×10^{24}
3C 84	64	1.7×10^6	1084	154	2.2×10^9	0.83	1.6×10^{24}
3C 120	55	2.0×10^6	884	112	7.6×10^9	0.23	3.0×10^{24}
PKS 0502-10	46	3.8×10^6	1075	185	1.3×10^{10}	0.32	2.5×10^{24}
B2 0722+30	50	2.3×10^6	525	105	4.8×10^9	0.24	2.2×10^{24}
B2 1318+34	58	9.4×10^6	572	222	8.0×10^9	0.68	2.3×10^{24}
PKS 1345+12	91	8.1×10^6	802	194	7.0×10^9	0.94	3.6×10^{24}
3C 293	40	3.6×10^6	1807	222	2.5×10^{10}	0.26	2.8×10^{24}
TXS 1506+345	54	8.4×10^6	860	227	1.6×10^{10}	0.46	2.9×10^{24}
Average	860 ± 460	0.45 ± 0.29	...

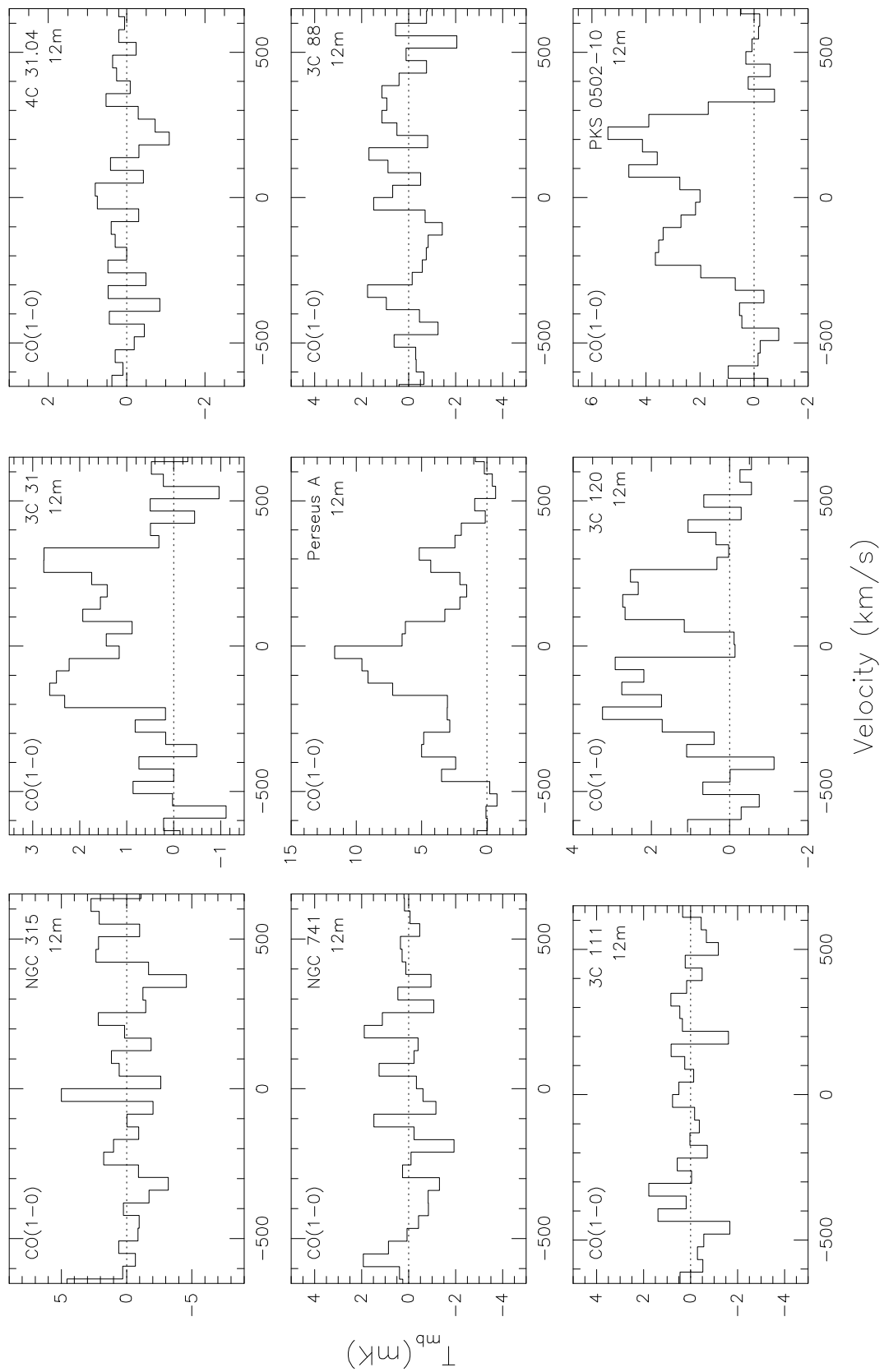


FIG. 1A.—

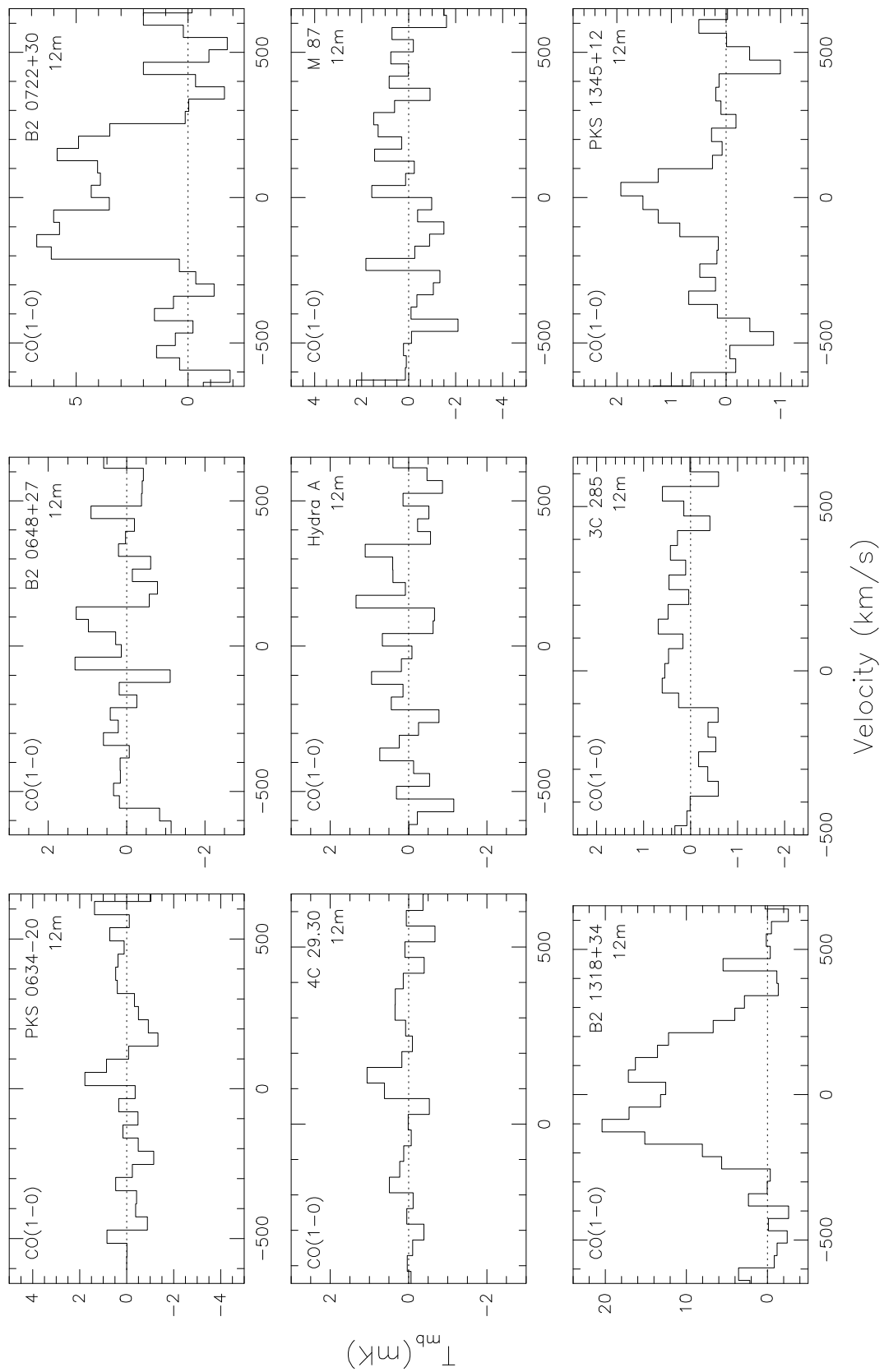


FIG. 1A.—

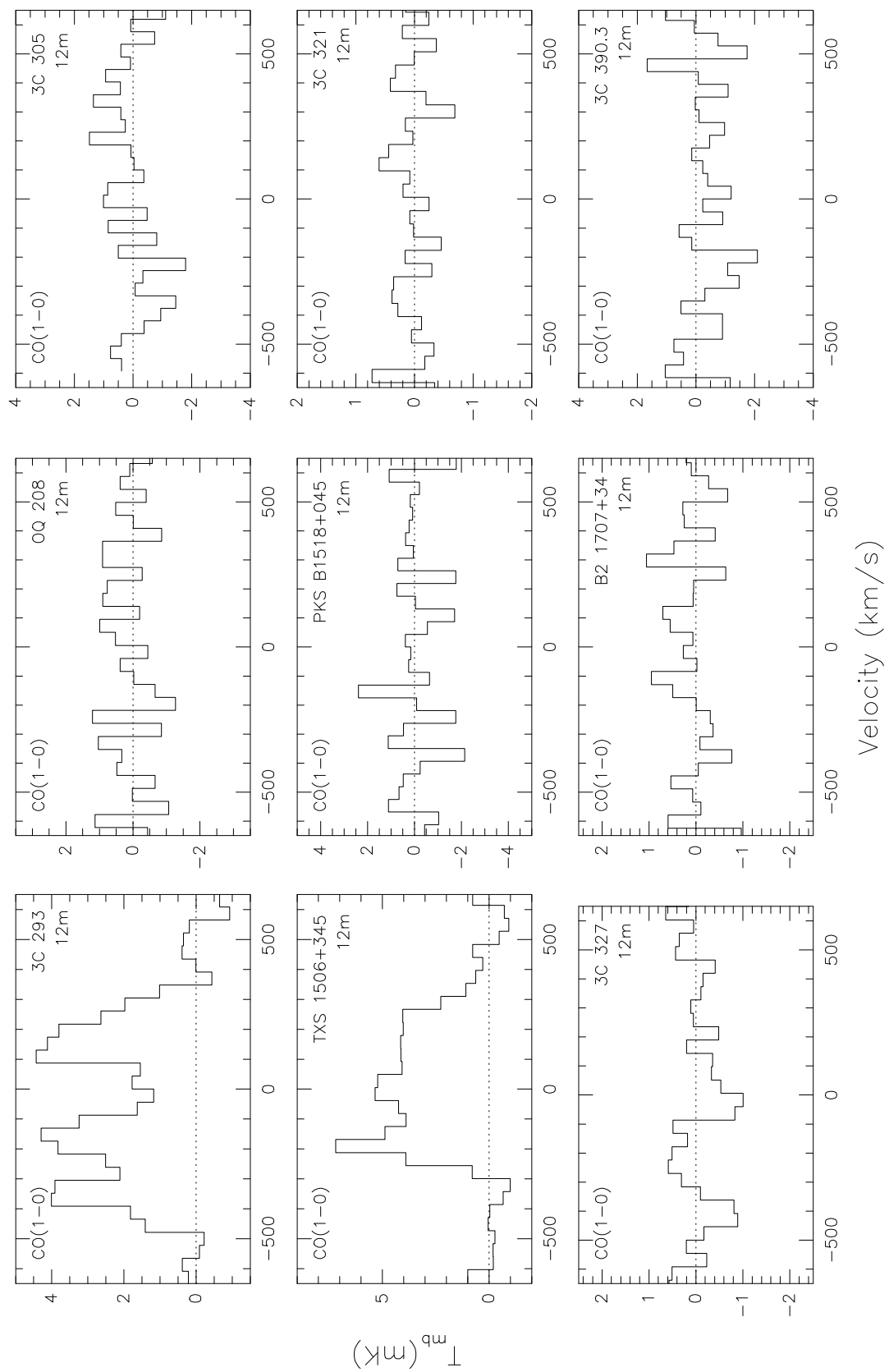


FIG. 1A.—

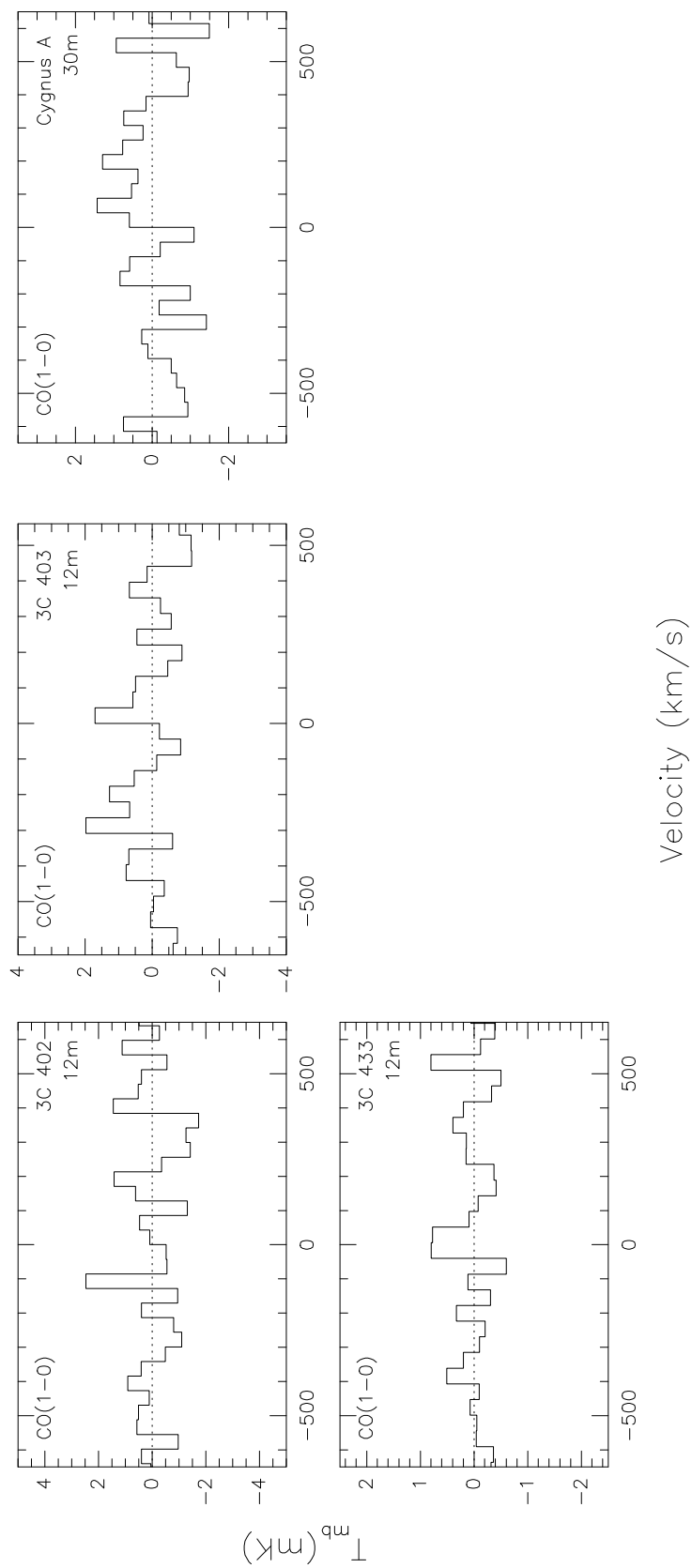


FIG. 1A.—

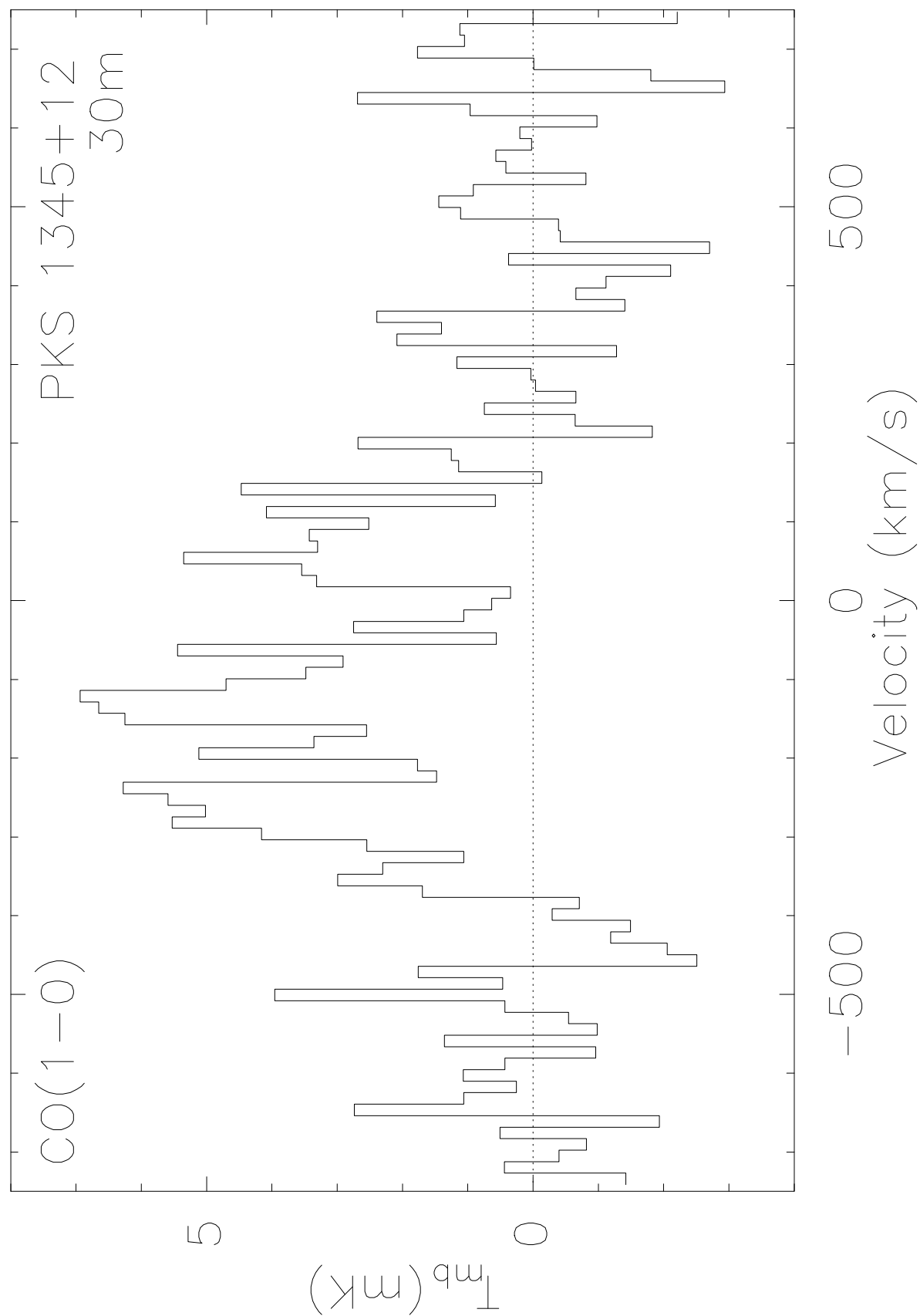


FIG. 1B.—

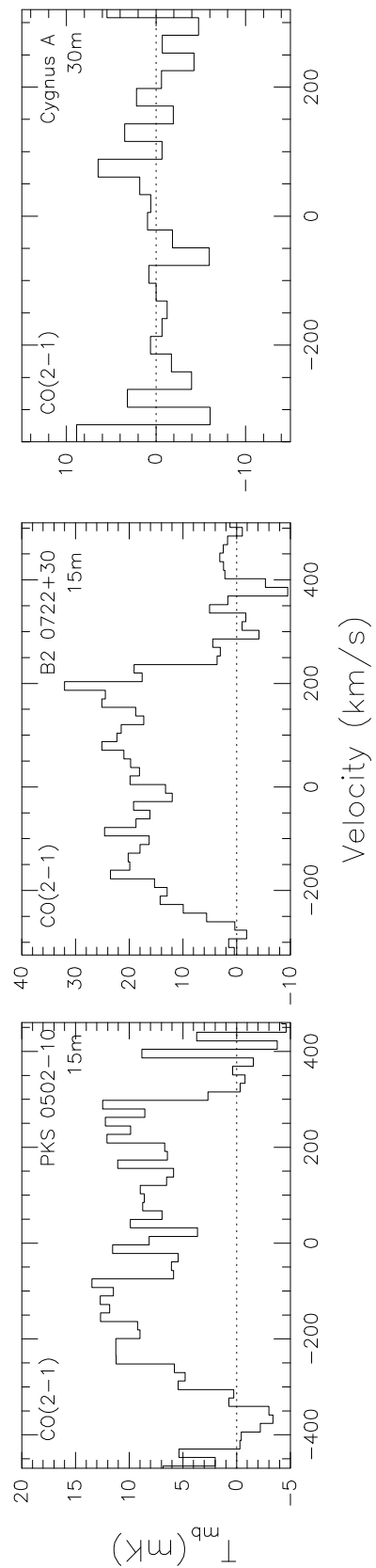


FIG. 2.—

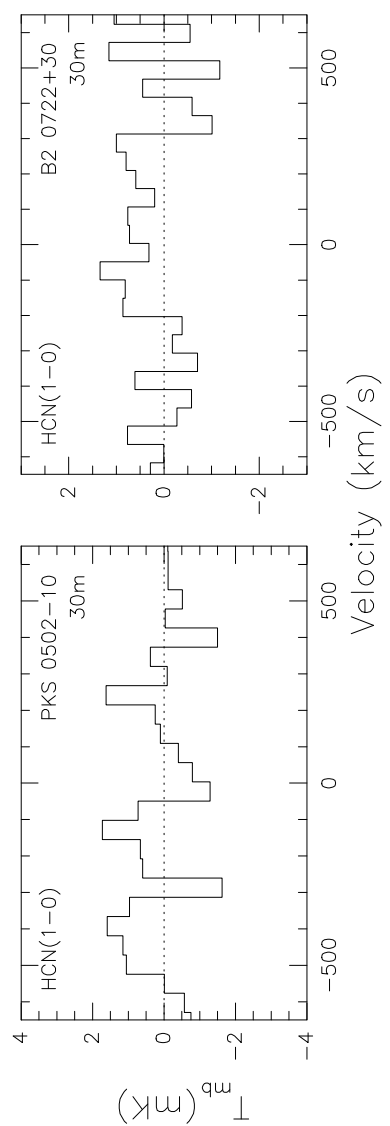


FIG. 3.—

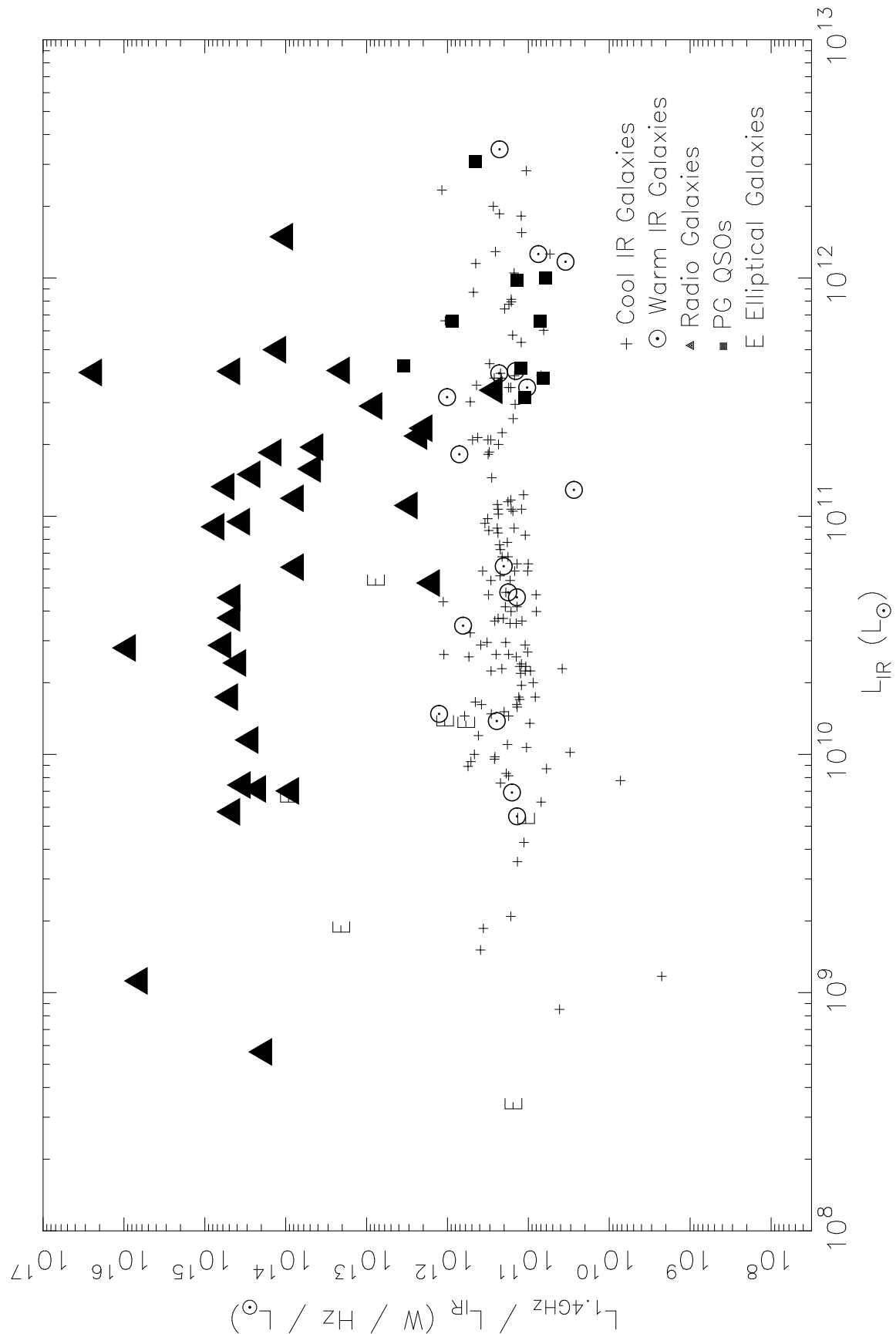


FIG. 5.—

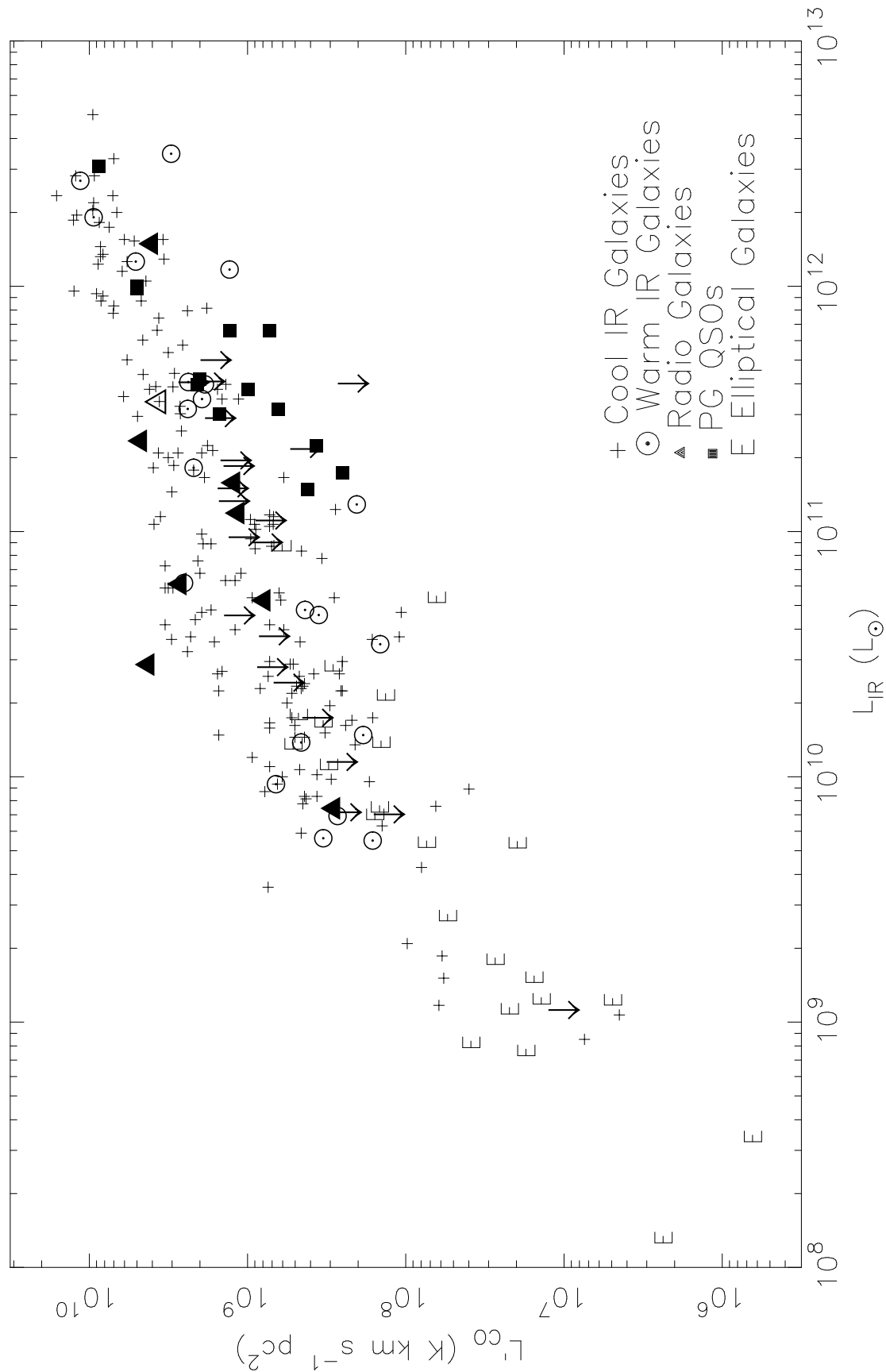


FIG. 6A.—

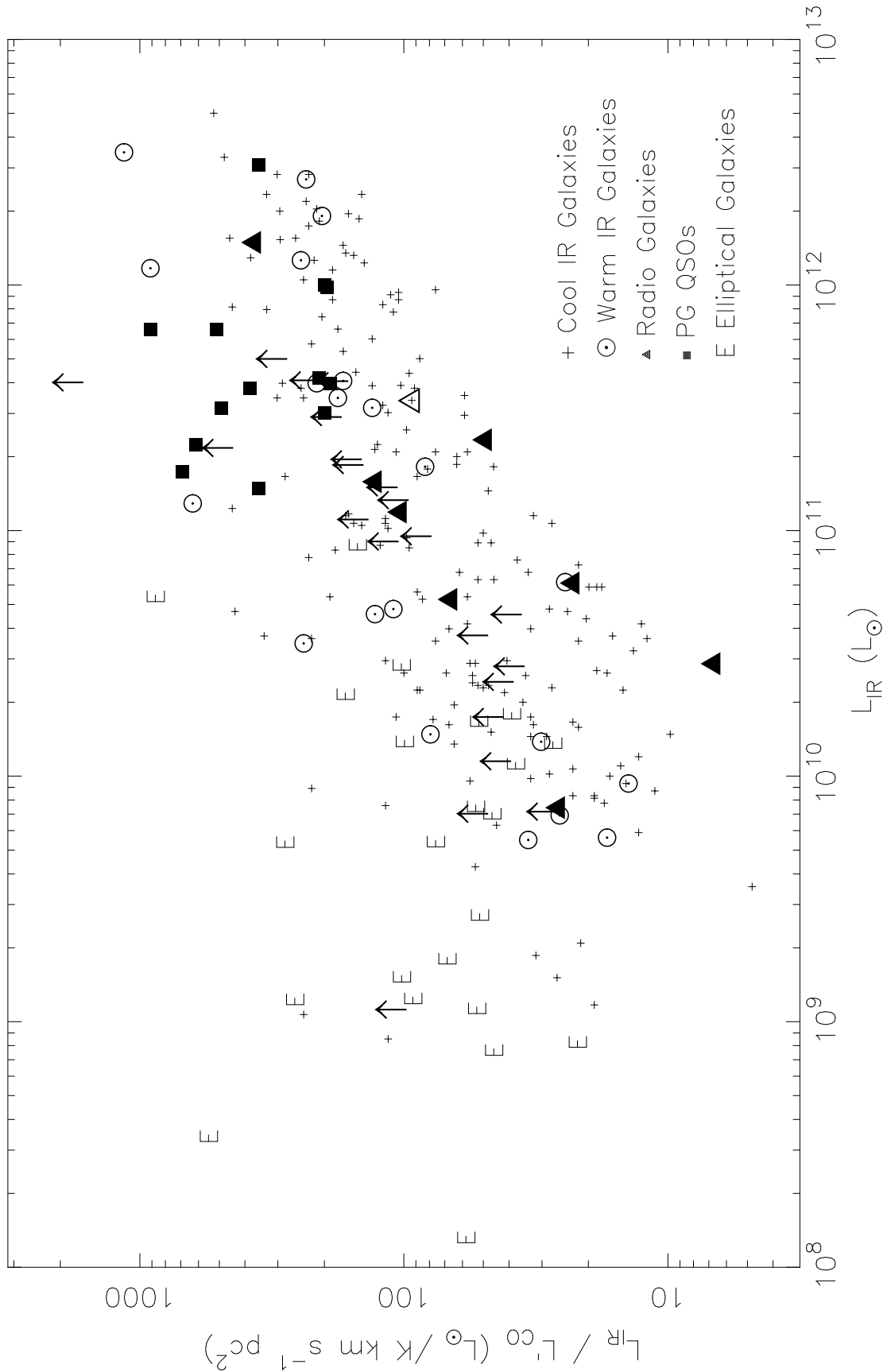


FIG. 6B.—

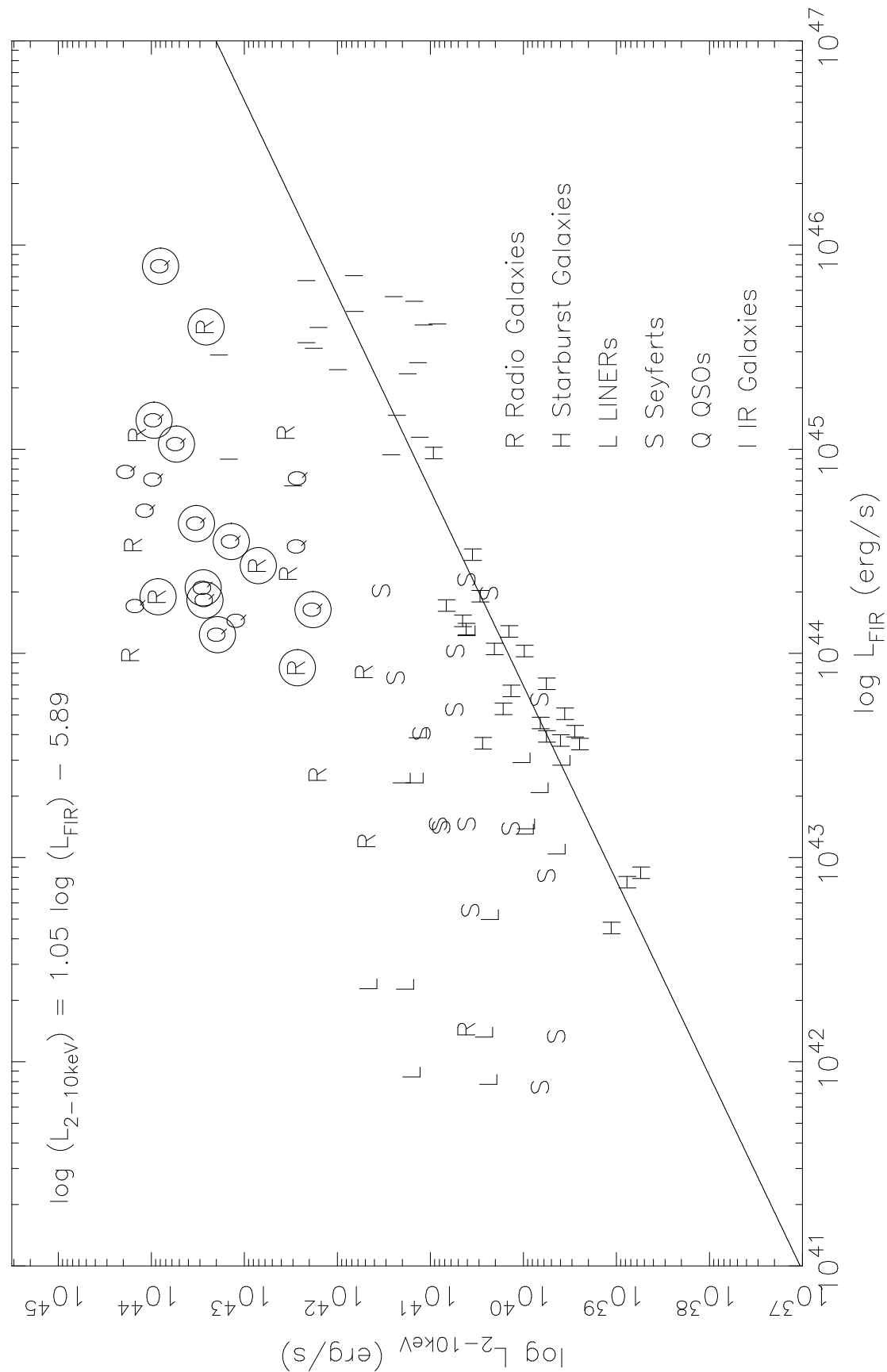


FIG. 7A.—

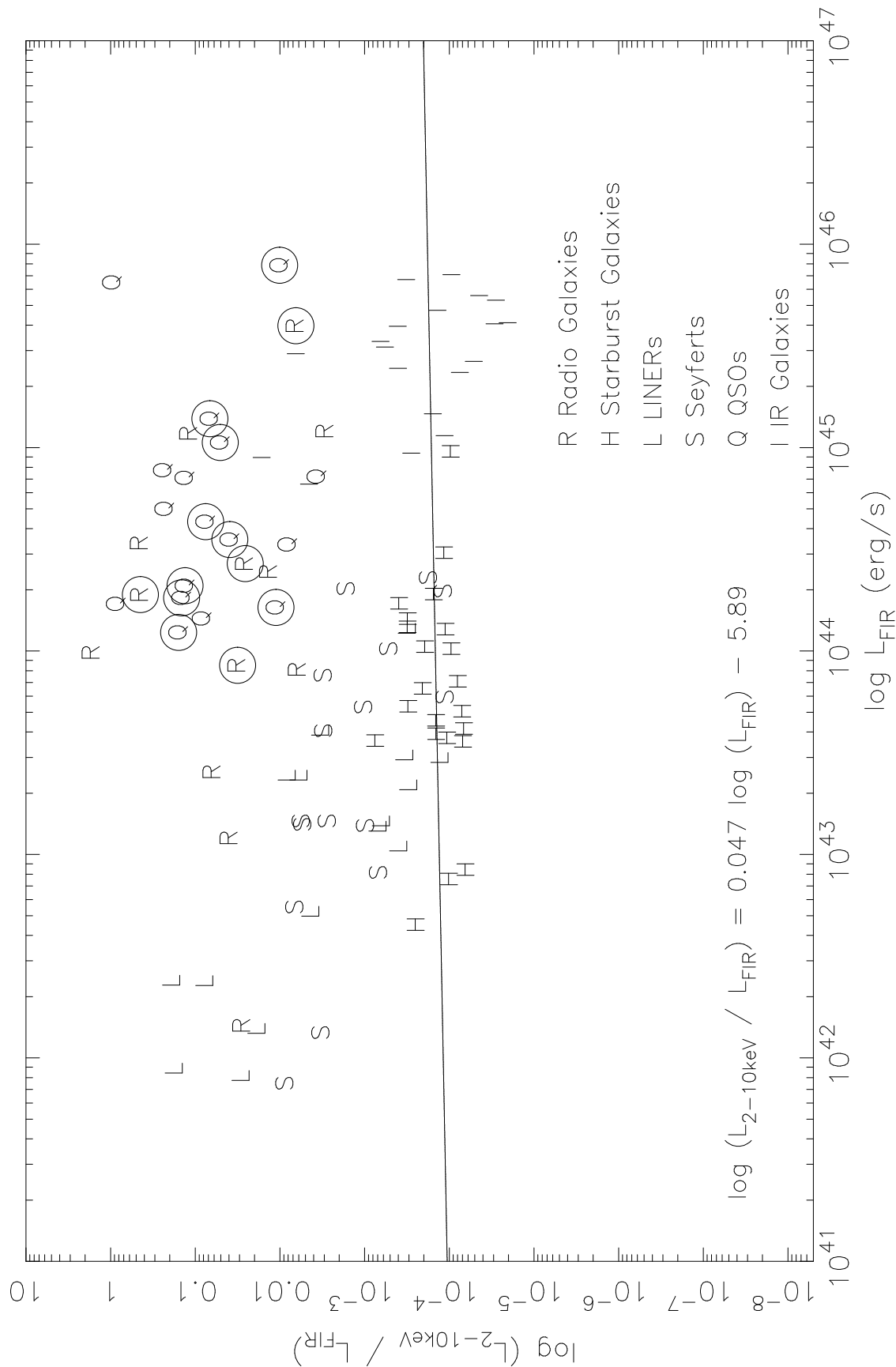


FIG. 7B.—

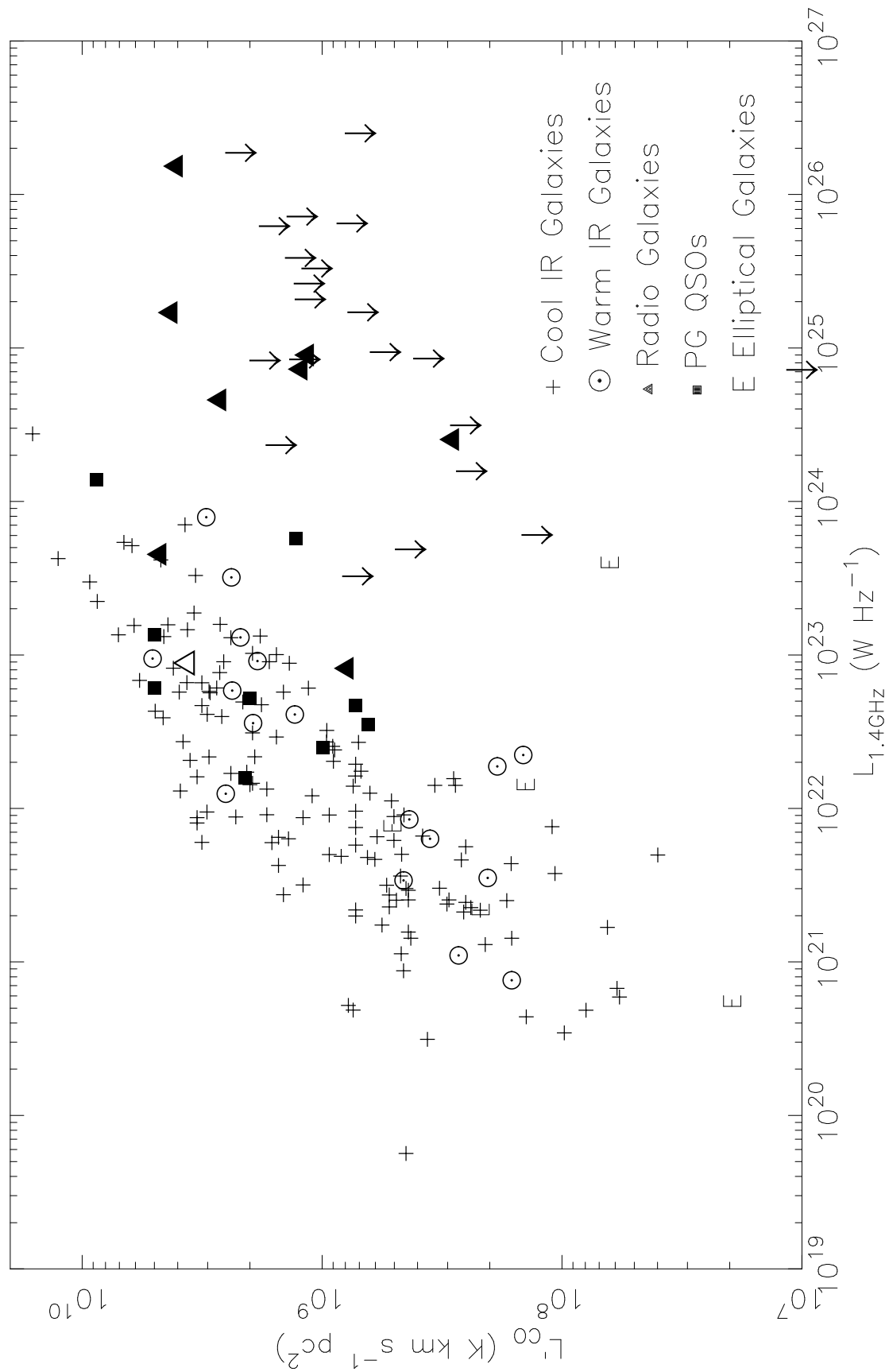


FIG. 8A.—

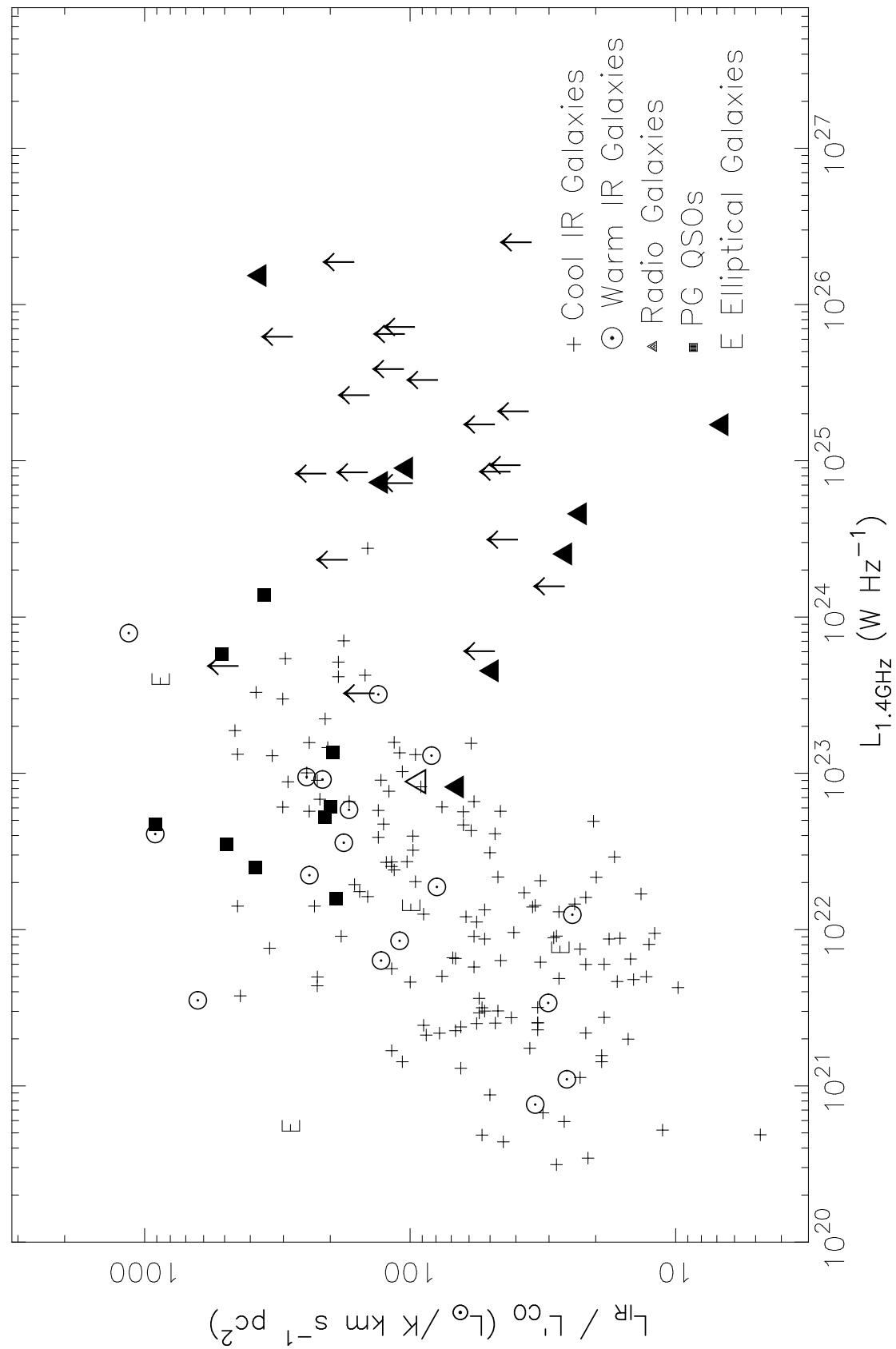


FIG. 8B.—

This figure "Evans.fig4.jpg" is available in "jpg" format from:

<http://arxiv.org/ps/astro-ph/0504604v1>